Current status of high-redshift 21-cm Intensity Mapping experiments

Presented by
Srijita Pal

Advanced 21-cm Cosmology, School and Workshop

National Institute of Science Education and Research, Bhubaneswar

December 19, 2023

Department of Physics, Indian Institute of Science, CV Raman Rd, Bengaluru, Karnataka 560012

Objective

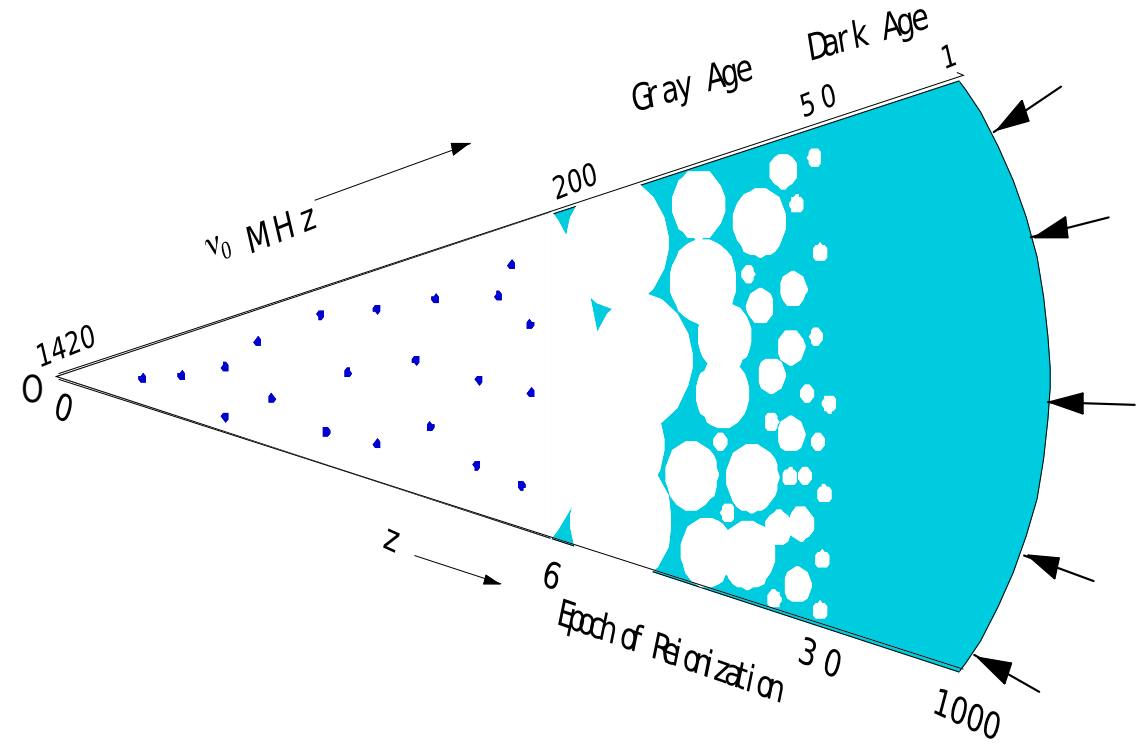

- Cosmic Dawn (CD), Epoch of Reionization (EoR) and post-EoR
- What do they tell us ?
- How to probe them ?

Bharadwaj and Ali, 2005

21-cm IM signal from EoR and post-EoR

- Excess brightness temperature fluctuations against the CMB

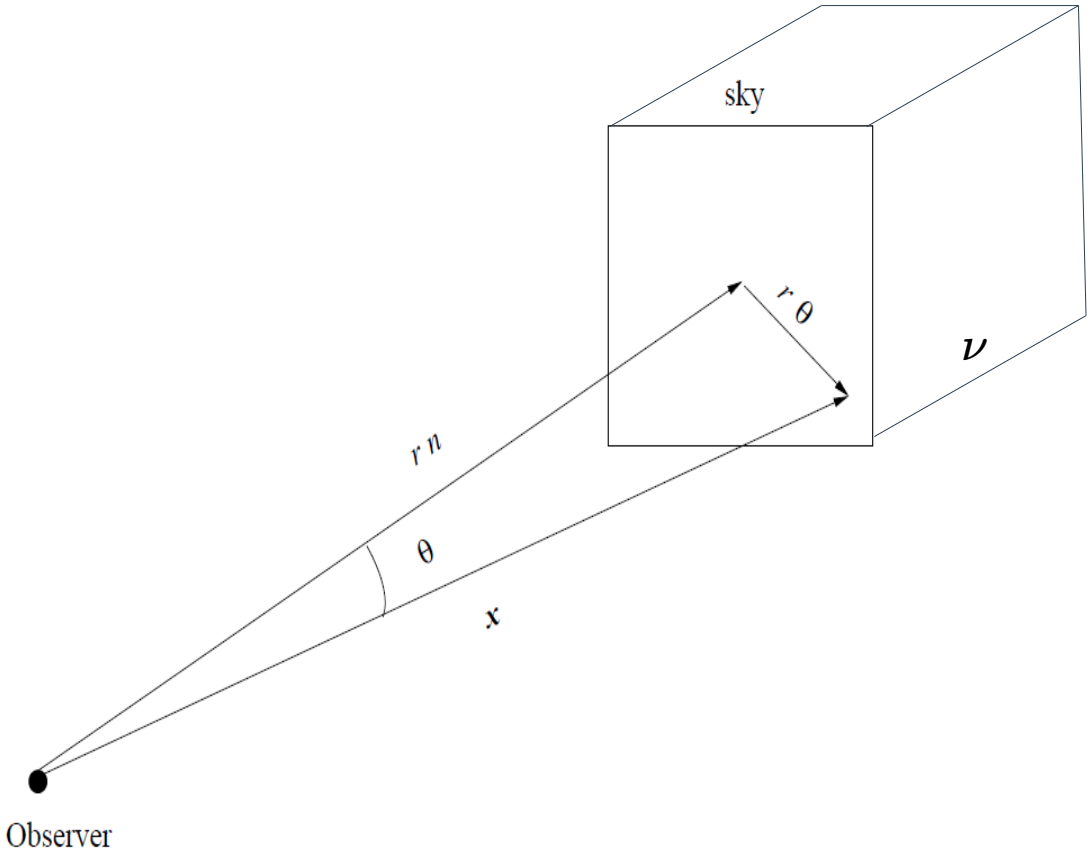

$$\delta T_{\rm b}(\hat{\mathbf{n}}, z) = \bar{T}(z) \times \eta_{\rm HI}(\hat{\mathbf{n}}, z)$$

where,

$$\bar{T}(z) = 4.0\,{\rm mK}(1+z)^2 \left(\frac{\Omega_b h^2}{0.02}\right)\left(\frac{0.7}{h}\right)\frac{H_0}{H(z)}$$

and

$$\eta_{\rm HI}(\hat{\mathbf{n}}, z) = \frac{\rho_{HI}}{\bar{\rho}_{\rm H}}\left(1-\frac{T_\gamma}{T_s}\right)\left[1-\frac{(1+z)}{H(z)}\frac{\partial v}{\partial r}\right]$$

Image Credits : BNS, 2001

Power Spectrum from EoR and post-EoR

- In Fourier Space, $$\eta_{\rm HI}(\hat{\mathbf{n}}, z) = \int \frac{d^3k}{(2\pi)^3} e^{-i\,\mathbf{k}\cdot r_\nu \hat{\mathbf{n}}} \tilde{\eta}_{\rm HI}(\mathbf{k}, z)$$

- We define the three dimensional power spectrum $P_{\rm HI}(\mathbf{k}, z)$ as

$$\langle \tilde{\eta}_{\rm HI}(\mathbf{k}, z)\, \tilde{\eta}^*_{\rm HI}(\mathbf{k}^{'}, z)\rangle = (2\pi)^3\, \delta^3_D(\mathbf{k}-\mathbf{k}^{'})\, P_{\rm HI}(\mathbf{k}, z)$$

- The Power Spectrum for the brightness temperature fluctuations is then given by,

$$\boxed{\langle \Delta\tilde{T}(\mathbf{k}, z)\, \Delta\tilde{T}^*(\mathbf{k}^{'}, z)\rangle = \bar{T}^2(z) \times (2\pi)^3\, \delta^3_D(\mathbf{k}-\mathbf{k}^{'})\, P_{\rm HI}(\mathbf{k}, z)}$$

- $P_{\rm HI}(\mathbf{k},z)$ related to model parameters

Status of 21-cm IM experiments so far

EoR

GMRT

LOFAR

MWA

HERA

SKA-LOW

EoR

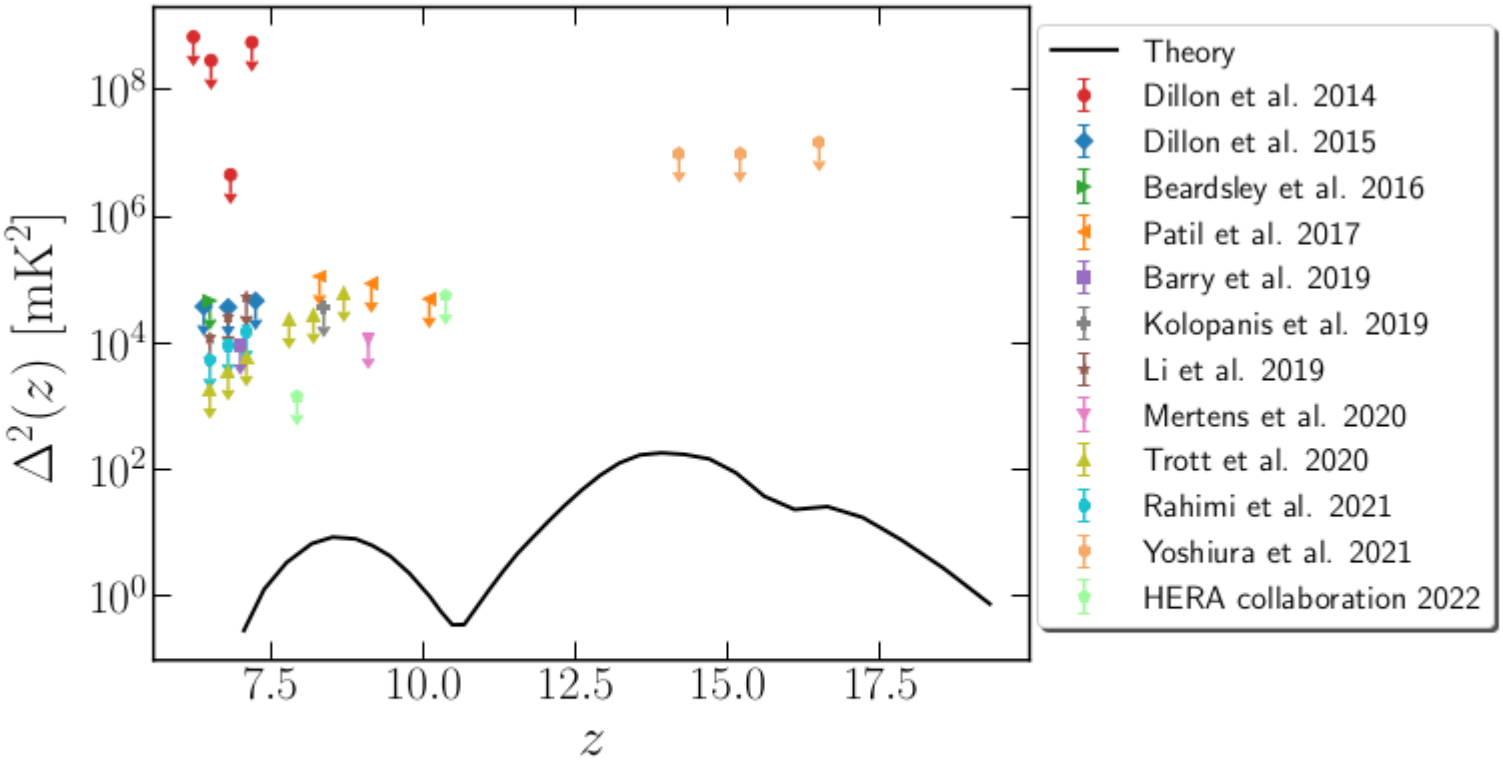

Figure 24. Shows a summery plot of the upper limits (in points) at $k \sim 0.1\,\mathrm{Mpc}^{-1}$, available to date, measured with the current instruments. The solid black line is a theoretical power spectrum estimated from a typical GRIZZLY simulation.

I.C. : Shaw et al., 2022

EoR

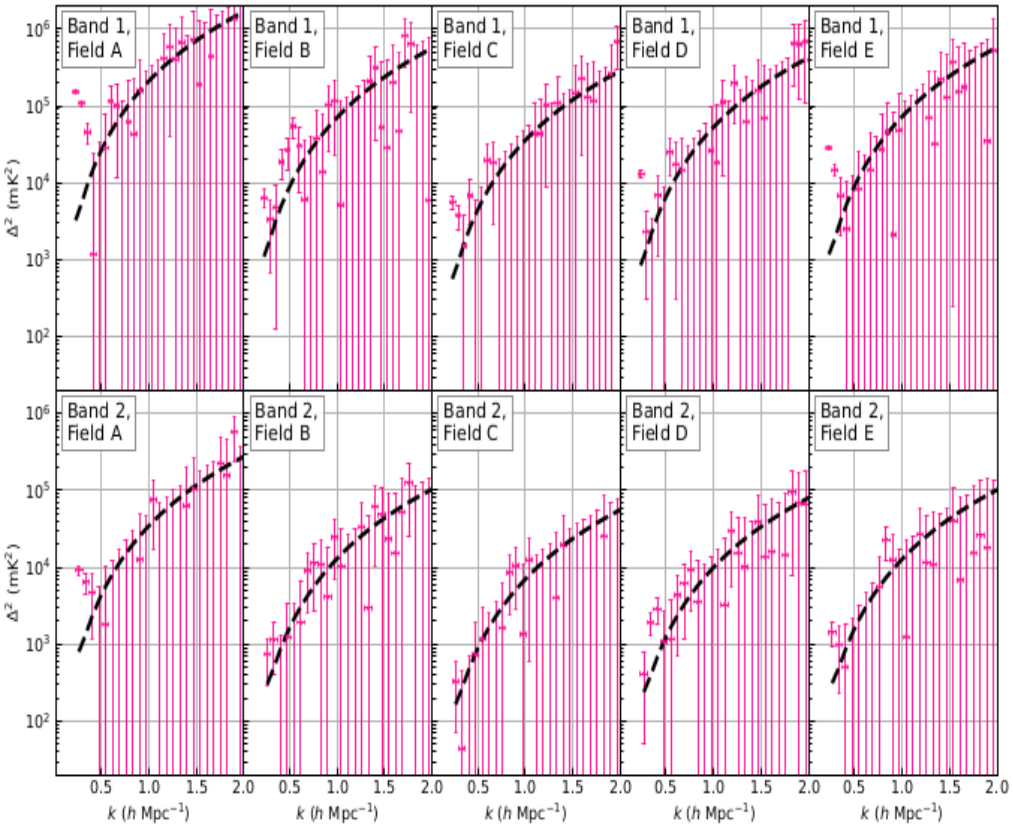

- The most sensitive upper limits to date on the 21 cm EoR power spectrum using 94 nights of observation using Phase I of HERA.
- EoR 21-cm power spectrum at z = 7.9 and 10.4.
- 2σ upper limits on the amplitude

  $\Delta^2(k) = 457\ \mathrm{mK}^2$ at $k = 0.34\ \mathrm{h\ Mpc^{-1}}$ for $z = 7.9$

  $\Delta^2(k) = 3{,}496\ \mathrm{mK}^2$ at $k = 0.36\ \mathrm{h\ Mpc^{-1}}$ for $z = 10.4$
- Limits provide updated constraints on the astrophysics of reionization and the cosmic dawn.

The HERA Collaboration, 2022

Post-EoR

Parkes

GBT

CHIME

GMRT/ uGMRT

Tianlai

Post-EoR

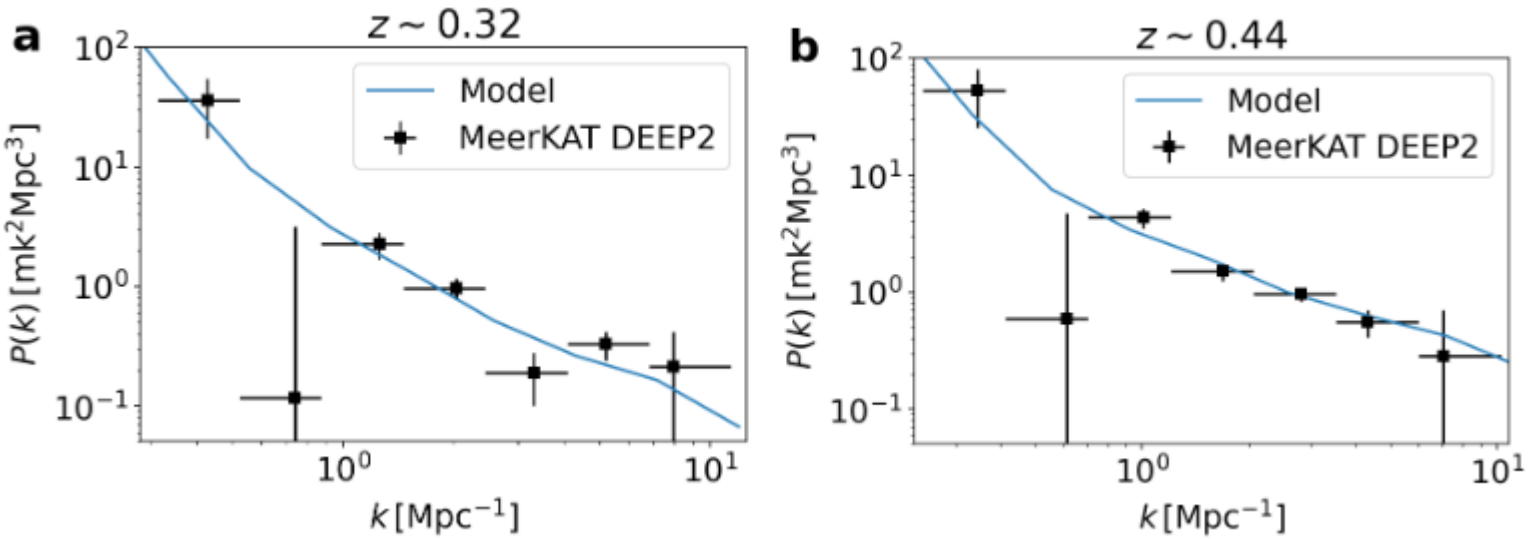

- The **first direct detection** of the post-EoR 21-cm power spectrum using 96 hours of observations with the L-band receivers of the new MeerKAT radio interferometer.
- Measurement of 21-cm power spectrum at z = 0.32 and 0.44 with high statistical significance of 8.0σ and 11.5σ respectively.
- The rms of the fluctuations of the HI distribution are constrained to be (0.44 ± 0.04) mK and (0.63 ± 0.03) mK respectively at scales of 1.0 Mpc.

Paul et al., 2023

Challenges for 21-cm Power Spectrum

Foregrounds

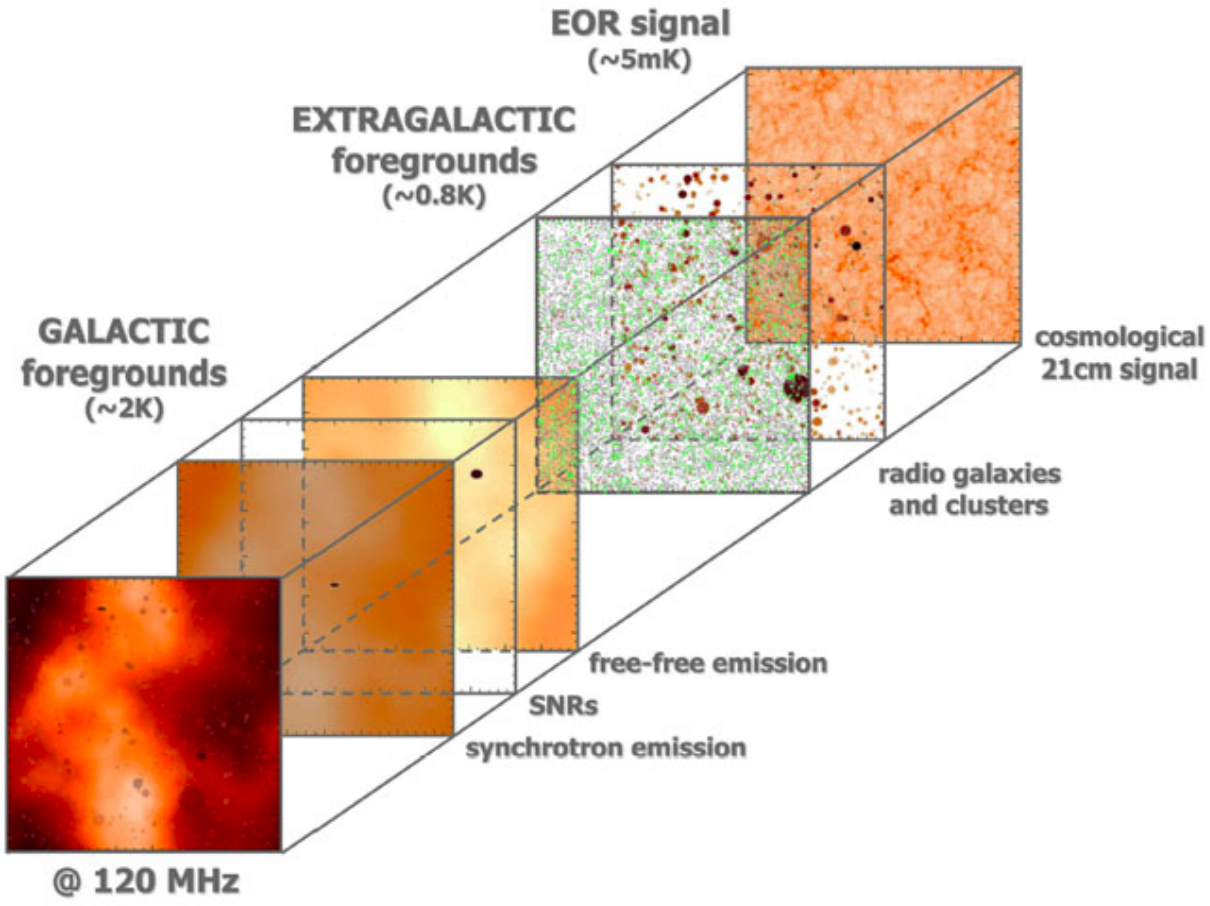

- What are foregrounds ?
- What constitutes the foregrounds ?
- DGSE and extra-galactic point sources 4-5 orders of magnitude larger than the 21-cm signal.

$$V(U,\nu) = S(U,\nu) + N(U,\nu) + F(U,\nu)$$

Frequency decorrelation

- Multi-frequency angular power spectrum, $C_\ell(\nu_a,\nu_b) = \langle\, V(U,\nu_a)\, V^*(U,\nu_b)\,\rangle$ modelled as,

$$C_\ell(\nu_a, \nu_b) = C_\ell \left(\frac{\nu_c}{\nu_a}\right)^\alpha \left(\frac{\nu_c}{\nu_b}\right)^\alpha$$

- Here, $C_\ell = A(1000/\ell)^\gamma$. For $\nu_b = \nu_a + \Delta\nu$,

$$C_\ell(\Delta\nu) \equiv C_\ell(\nu_a, \nu_a + \Delta\nu) \approx C_\ell \left(\frac{\nu_c}{\nu_a}\right)^{2\alpha} \left(1 - \frac{\alpha\,\Delta\nu}{\nu_a}\right)$$

Frequency decorrelation

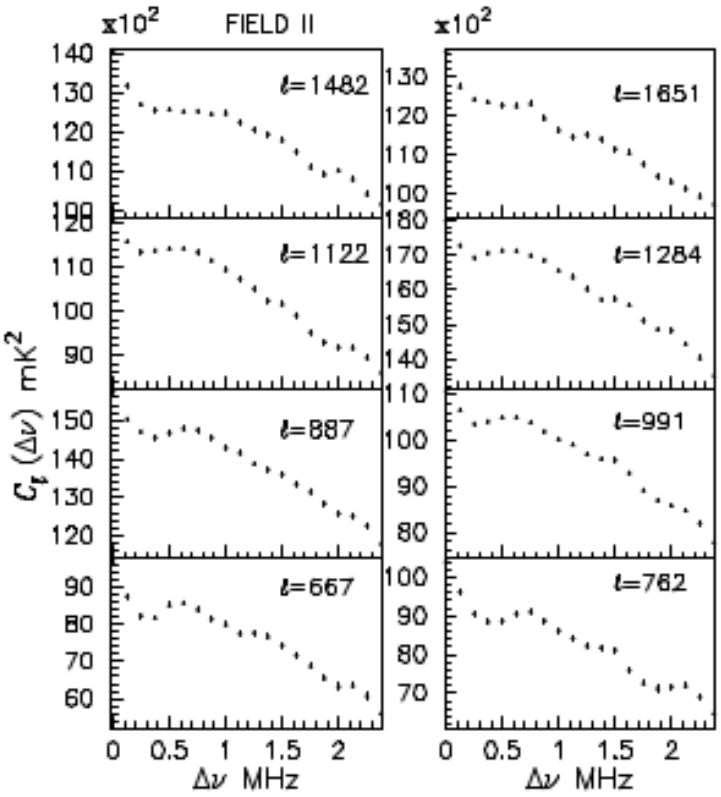

Foregrounds

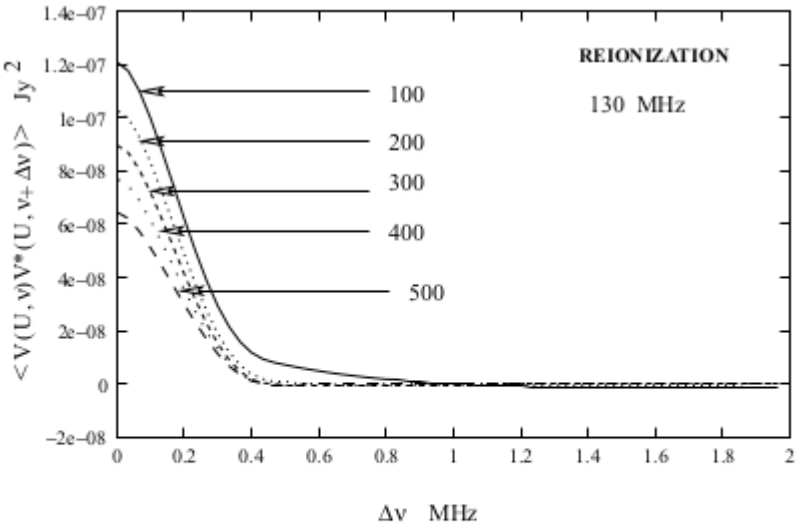

Figure 7. This shows the correlation between the visibilities $V(U, \nu)$ and $V(U, \nu + \Delta\nu)$ expected for the same baseline U at two slightly different frequencies. The result are shown for different values of U (shown in the figure) for the 130-MHz band.

21-cm signal

I.C.: Ghosh et al., 2012, Bharadwaj & Ali, 2005

Foreground wedge, EoR window, Avoidance and Spectral leakage

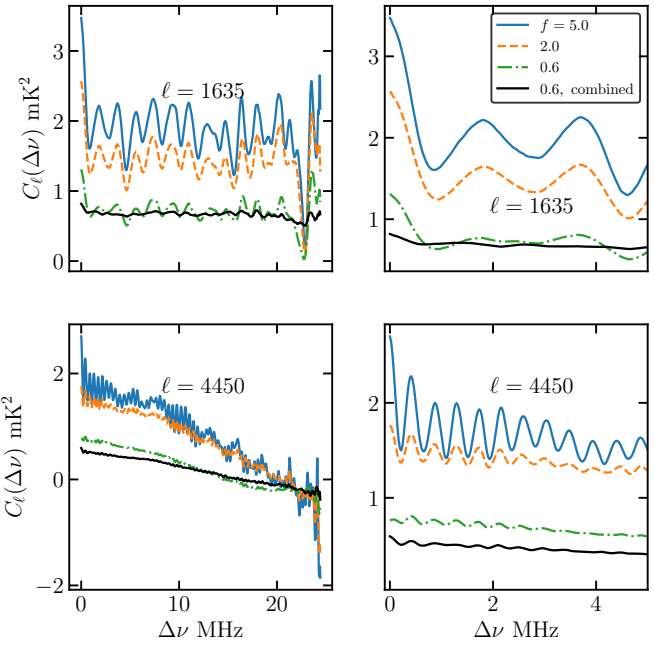

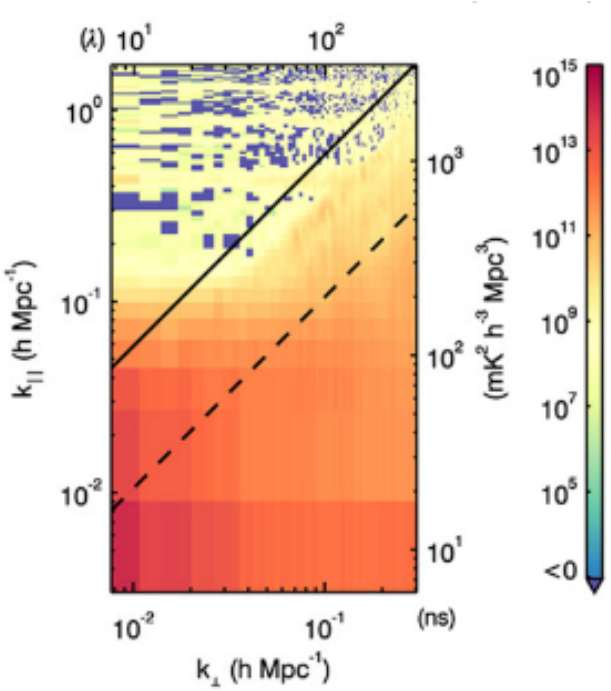

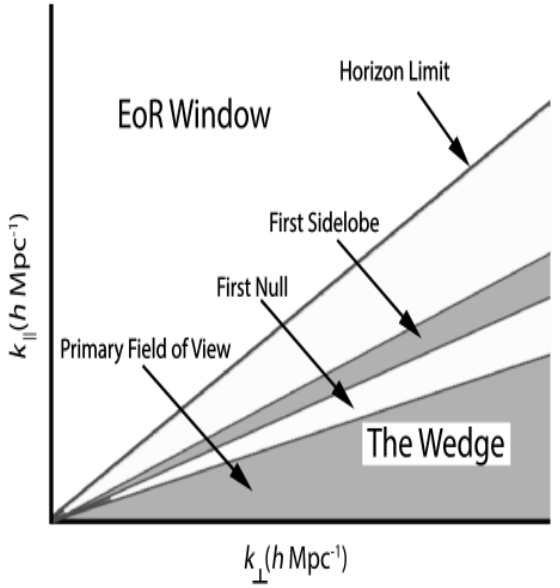

Instrumental systematics due to Gain Variations, Primary Beam

I.C.: Pober et al., 2016

Foreground Removal

- Parametrized fits (Di Matteo et al. 2002; Santos et al. 2005; Wang et al. 2006; Liu et al. 2009a; Liu et al. 2009b; Bowman et al. 2009)

- Non-parametric fits (Harker et al. 2009a; Cho et al. 2012; Mertens et al. 2018 - GPR)

- Mode projection (Pindor et al. 2011; Bernardi et al. 2011; Sullivan et al. 2012; Liu & Tegmark 2012 – PCA; Paciga et al. 2013; Shaw et al. 2014; Zheng et al. 2017A; Chapman et al. 2012; Wolz et al. 2014, 2017b – ICA; Chapman et al. 2013 - GMCA)

- Mode weighting (Liu & Tegmark 2011)

Liu & Shaw, 2019

Other factors for detection of the power spectrum

- Instrumental systematics due to Gain Variations, Primary Beam
- Polarization leakage
- Mutual Coupling
- Ionosphere
- Radio frequency interference
- Signal loss
- Excess Variance
- Accuracy required in IM experiments

Our Efforts

21-cm IM with the Tapered Gridded Estimator (TGE)

Work done in collaboration with

Somnath Bharadwaj, Kh. Md. Asif Elahi, Sk. Saiyad Ali, Samir Choudhuri, Abhik Ghosh, Arnab Chakraborty, Abhirup Datta, Nirupam Roy, Madhurima Choudhury, Prasun Dutta

Wide-Field Foregrounds

- Effects wide-field foregrounds
- Higher angular distance, higher k modes contamination
- Spectral leakage
- Difficulties in removing wide-field foregrounds

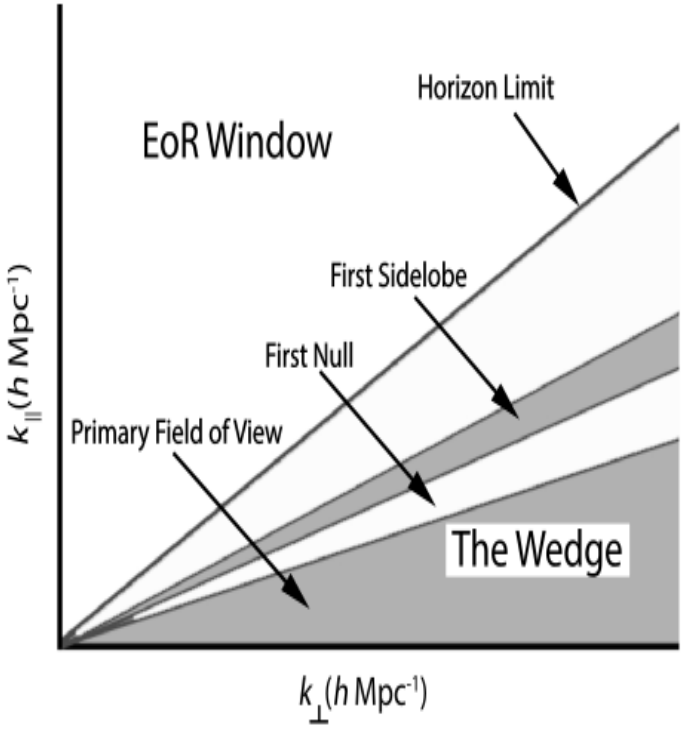

I.C. : Pober et al., 2016

Flagging

- Dealing with the flagged data

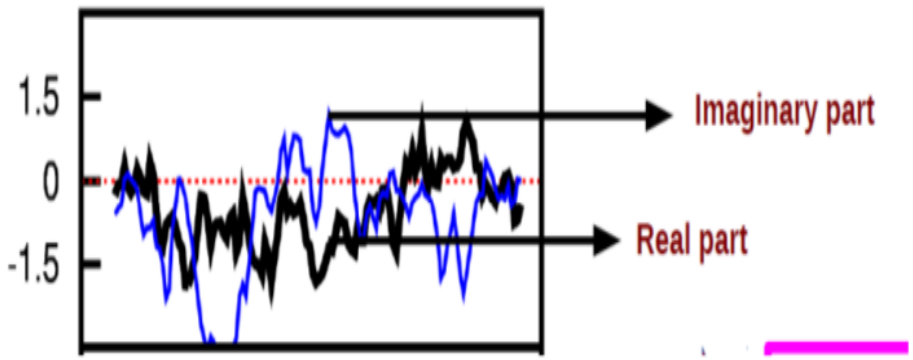

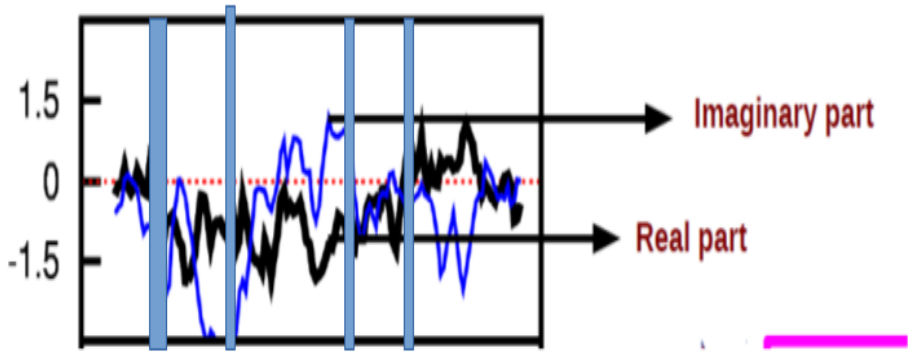

- Remember power spectrum estimated in the Fourier domain

$$\langle \Delta\tilde{T}(\mathbf{k}, z)\, \Delta\tilde{T}^{*}(\mathbf{k}', z) \rangle = \bar{T}^{2}(z) \times P_{\rm HI}(\mathbf{k}, z)$$

Flagged: Convolution with FT of the flagged window function

I.C. : Sarkar et al., 2017

Why use TGE ??

- Present an estimator for the detection of the 21-cm power spectrum from EoR and post-EoR from radio interferometric observations whose salient features are as follows,

  (a) Effectively tapers the sky response, to suppress the wide-field foreground contributions from outside the main lobe of the antenna response

  (b) Subtracts the positive definite noise bias to yield an unbiased estimate of the measured quantities (e.g. power spectrum)

  (c) Reduces the computational load

  (d) Deals with the flagged data without much increase in computational load.

MAPS and Power Spectrum

- Decompose in spherical harmonics,

$$\delta T_{\rm b}(\hat{\boldsymbol{n}},\,\nu) = \sum_{\ell,m} a_{\ell {\rm m}}(\nu)\, Y_{\ell}^{\rm m}(\hat{\boldsymbol{n}})$$

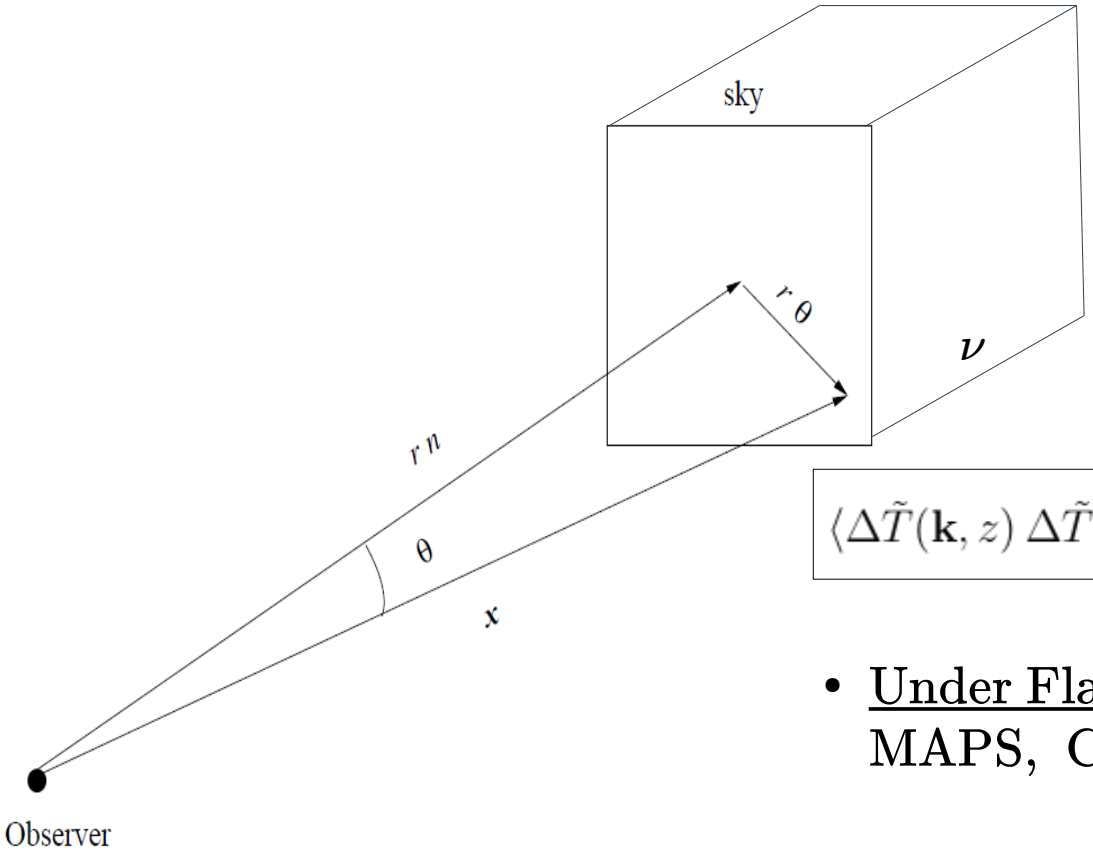

- Multi-frequency angular power spectrum (MAPS)

$$C_{\ell}(\nu_a, \nu_b) = \left\langle a_{\ell {\rm m}}(\nu_a)\, a^{*}_{\ell {\rm m}}(\nu_b) \right\rangle$$

- Power Spectrum

$$\langle \Delta\tilde{T}(\mathbf{k}, z)\, \Delta\tilde{T}^{*}(\mathbf{k}', z) \rangle = \bar{T}^2(z) \times (2\pi)^3\, \delta_D^3(\mathbf{k} - \mathbf{k}')\, P_{\rm HI}(\mathbf{k}, z)$$

- Under Flat sky approximaton,

MAPS, $C_{\ell}(\Delta\nu)$ ⟷ (F.T.) Power Spectrum

I.C. : BNS, 2001

Estimating the MAPS : Gridding and Tapering

Visibilities :

$$\mathcal{V}_i = \left(\frac{\partial B}{\partial T}\right) \int d^2U\, \tilde{a}\,(\mathbf{U}_i - \mathbf{U})\;\; \Delta\tilde{T}(\mathbf{U}) + \mathcal{N}_i$$

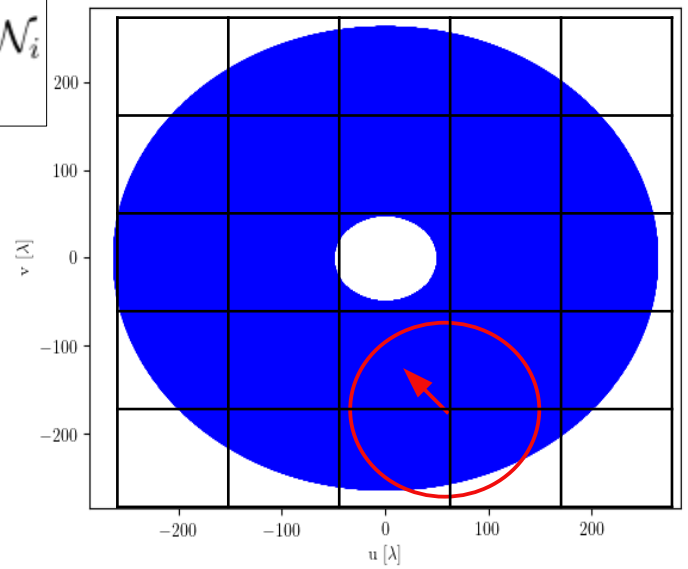

Gridded Visibilities

$$\mathcal{V}_{cg}(\nu_a) = \sum_i \tilde{w}(\mathbf{U}_g - \mathbf{U}_i)\, \mathcal{V}_i(\nu_a)\, F_i(\nu_a)$$

F. T.

$$\mathcal{W}(\theta) = e^{-\theta^2/\theta_w^2}$$

Tapering the GMRT primary beam

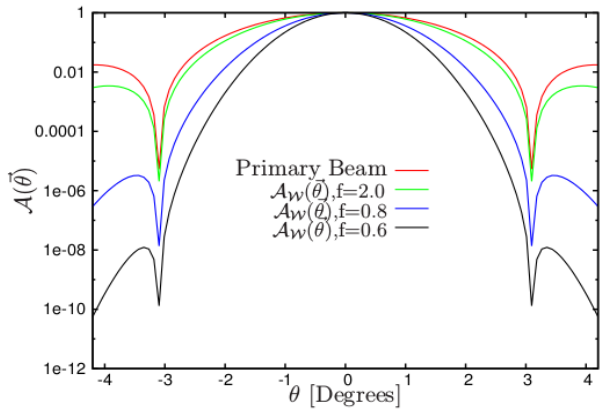

$$\mathcal{A}(\vec{\theta},\, \nu) = \left[\left(\frac{2\lambda}{\pi\theta D}\right) J_1\left(\frac{\pi\theta D}{\lambda}\right)\right]^2$$

$$\mathcal{W}(\theta) = e^{-\theta^2/\theta_w^2}$$

$$\theta_w = f\theta_0$$

I.C. : Choudhuri et al., 2016

The Tapered Gridded Estimator for MAPS

$$\hat{E}_g(\nu_a,\nu_b) = M_g^{-1}(\nu_a,\nu_b)\,\mathcal{R}e\left[\mathcal{V}_{cg}(\nu_a)\,\mathcal{V}_{cg}^{*}(\nu_b) - \sum_i F_i(\nu_a)F_i(\nu_b)\mid \tilde{w}(\mathbf{U}_g-\mathbf{U}_i)\mid^2 \mathcal{V}_i(\nu_a)\mathcal{V}_i^{*}(\nu_b)\right]$$

Normalization

Noise-bias

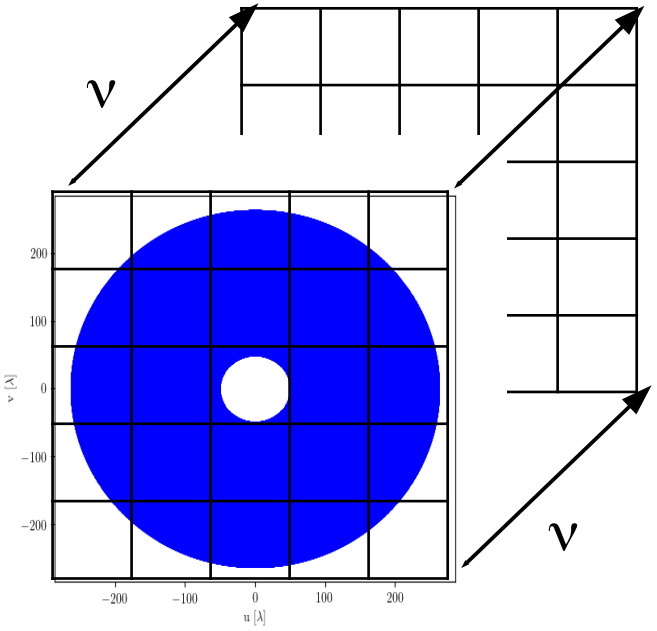

Normalization

UMAPS : $C_\ell(\nu_a,\nu_b) = 1$

$$M_g(\nu_a,\nu_b) =$$

$$\mathcal{R}e\left[\mathcal{V}_{cg}(\nu_a)\,\mathcal{V}_{cg}^{*}(\nu_b) - \sum_i F_i(\nu_a)F_i(\nu_b)\mid \tilde{w}(\mathbf{U}_g-\mathbf{U}_i)\mid^2 \mathcal{V}_i(\nu_a)\mathcal{V}_i^{*}(\nu_b)\right]$$ UMAPS

$$\langle \hat{E}_g(\nu_a,\nu_b)\rangle = C_{\ell_g}(\nu_a,\nu_b)$$ → Unbiased Estimates at $\ell_g = 2\pi U_g$

Power Spectrum Estimation

$$P(k_\perp,\ k_\parallel) = r^2\, r' \int_{-\infty}^{\infty} d(\Delta\nu)\, e^{-ik_\parallel r' \Delta\nu}\, C_\ell(\Delta\nu)$$

$$C_\ell(\nu_a, \nu_b) = C_\ell(\Delta\nu) \text{ where } \Delta\nu = \mid \nu_b - \nu_a \mid$$

Values estimated at :

$$C_\ell(n\,\Delta\nu_c) \text{ where } -(N_c - 1) \leqslant n \leqslant (N_c - 1) \text{ with } C_\ell(n\,\Delta\nu_c) = C_\ell(-n\,\Delta\nu_c).$$

$$C_\ell(n\,\Delta\nu_c) = \sum_m \mathbf{A}_{nm}\, P(k_\perp, k_{\parallel m}) + [\text{Noise}]_n \qquad \text{where } n,\ m\ \epsilon\,[0, N_c - 1].$$

Maximum Likelihood estimate of Power spectrum

$$P(k_\perp, k_{\parallel m}) = \sum_n \{[\mathbf{A}^\dagger \mathbf{N}^{-1} \mathbf{A}]^{-1} \mathbf{A}^\dagger \mathbf{N}^{-1}\}_{mn} C_\ell(n\Delta\nu_c) \quad \text{with } k_{\parallel m} = m \times [\pi / r'_c\, \Delta\nu_c (N_c - 1)]$$

N -> Noise covariance matrix

Cylindrical ans Spherical Power Spectrum

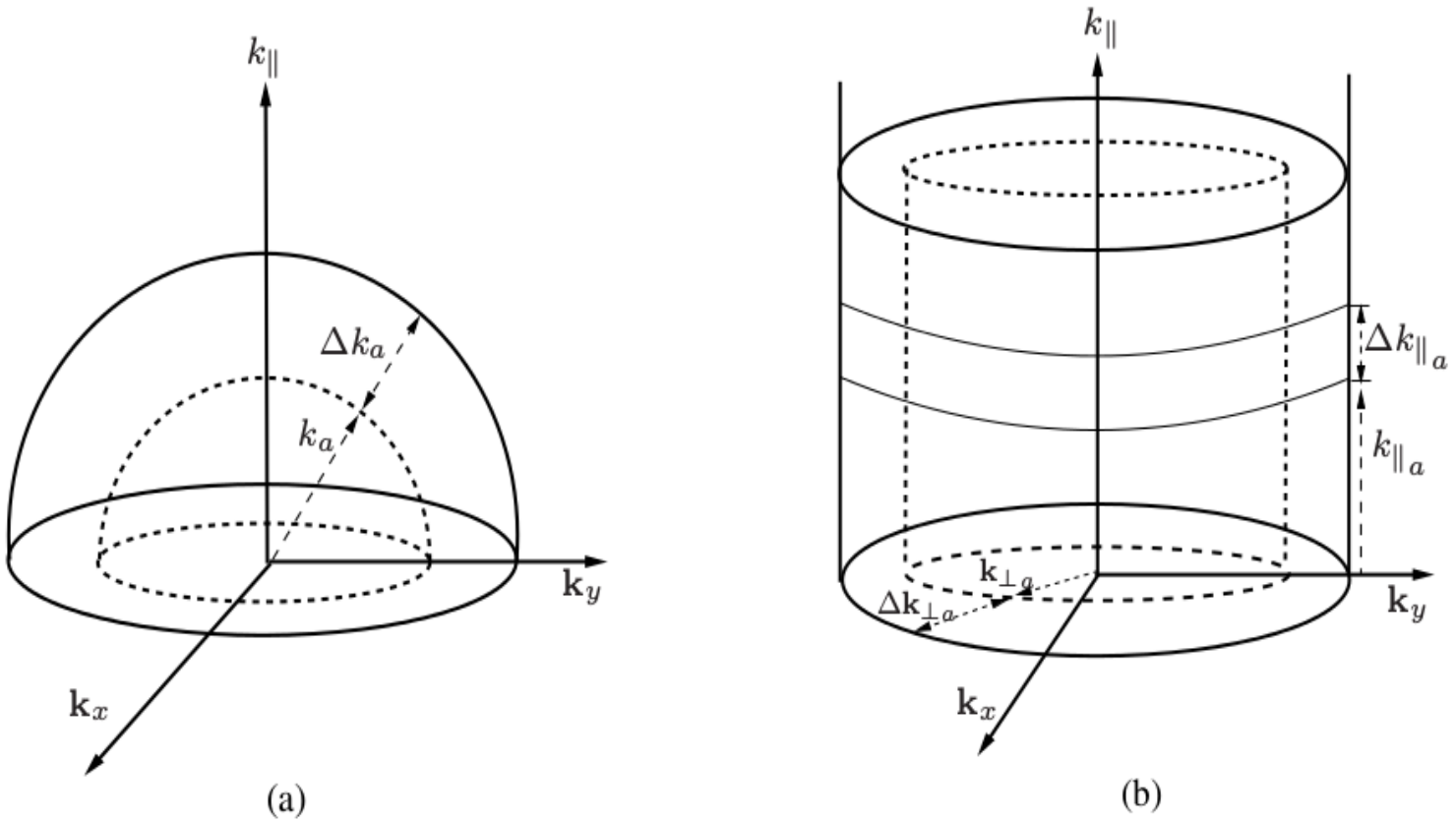

Figure 4. This shows a typical bin for respectively calculating the Spherical Power Spectrum (left) and the Cylindrical Power Spectrum (right).

I.C. : Choudhuri et al., 2016b

Validation of the Tapered Gridded Estimator

GMRT

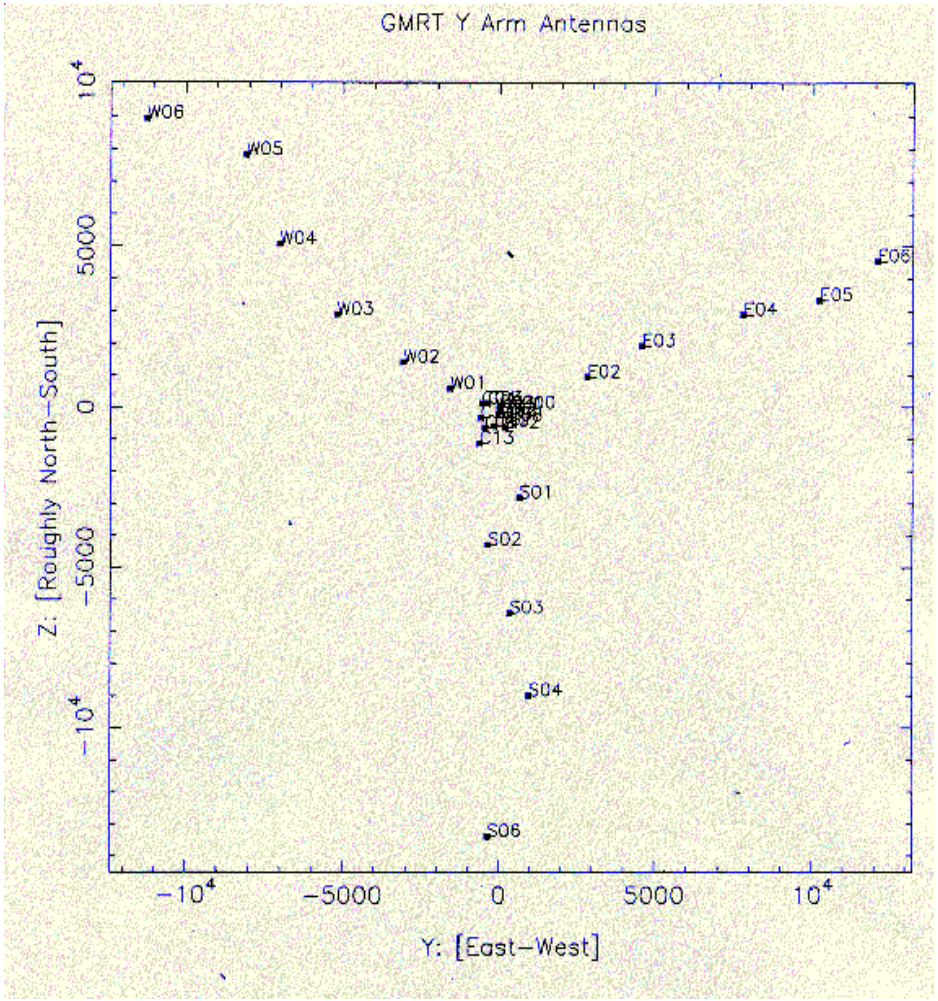
GMRT Y Arm Antennas
W06
W05
W04
W03
W02
W01
E01
E02
E03
E04
E05
E06
S01
S02
S03
S04
S06
10^4
5000
0
−5000
−10^4
Z: [Roughly North−South]
Y: [East−West]

Specifications for the simulations

Table 1: Observation summary

Number of antennas	30
Diameter	45 m
Central Frequency	150 MHz
Number of Channels	257
Bandwidth	$\approx$ 16 MHz
Total observation time	8 h
Integration time	16 s
Target field $(\alpha, \delta)_{2000}$	$(10^h46^m00^s,$ $+59°00'59.9'')$

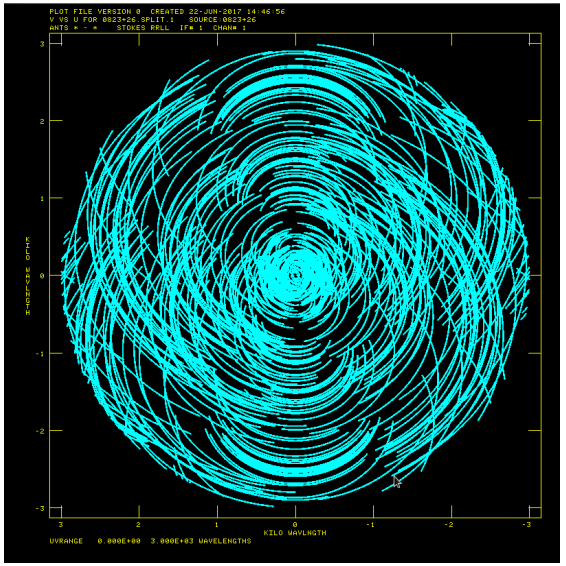

$$| \mathbf{U_i} | \leq 3000\ \lambda$$

Model, Noise and flagging in the simulation

- **Model for the signal:** $P^m(k) = (k/k_0)^n \,\mathrm{mK}^2\,\mathrm{Mpc}^3$.

  $k_0 = (1.1)^{-1/2}\,\mathrm{Mpc}^{-1}$ and $n = -2$.

- Simulated on a $[2048]^3$ grid with resolution ΔL=1.073 Mpc to match the frequency resolution $\Delta\nu_c$ =62.5 kHz. FoV around 5 times the FWHM of GMRT.

- **Noise:** Gaussian random variable $R = \sigma_N/\sigma_{sky} = 10$

Model, Noise and flagging in the simulation

- **Flagging:** We have considered simulations both with and without flagging. For each baseline we have generated random integers in the range $1 \leqslant a \leqslant N_c$ and flagged the corresponding channels. We have carried out simulations for various values of $f_{\rm FLAG}$ (the fraction of flagged channels) in the range $0 \leqslant f_{\rm FLAG} \leqslant 0.8$.

Results

$$C_\ell(\Delta\nu) = \frac{1}{\pi r^2}\int_0^\infty dk_\parallel \cos(k_\parallel r' \Delta\nu) P(k_\perp, k_\parallel)$$

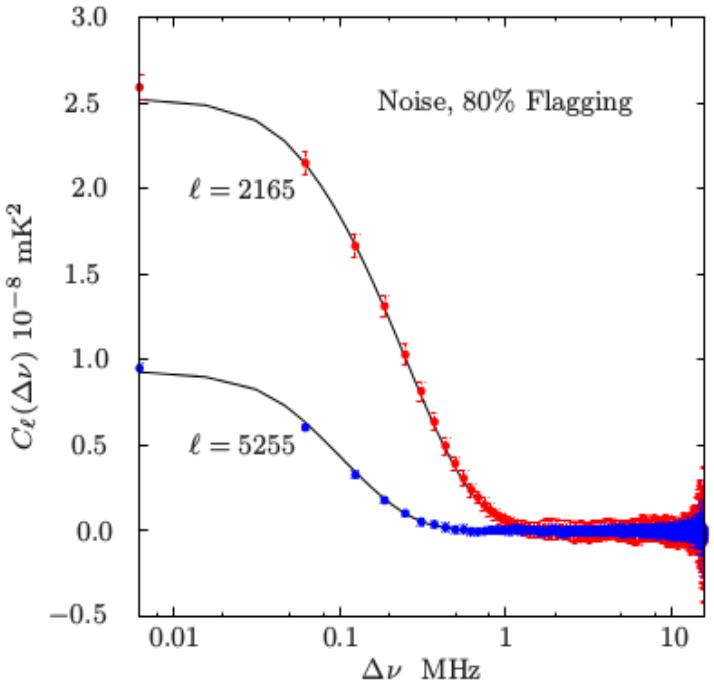

- The results from the simulations are in agreement with the theoretical predictions.
- Visually indistinguishable from the results from simulations with no noise and no flagging, or those with 20%, 40% and 60% flagging.

Figure 1. This shows $C_\ell(\Delta\nu)$ as a function of $\Delta\nu$ for two values of ℓ. The data points with $1-\sigma$ error-bars are estimated from 24 realizations of the simulations. Note that the $\Delta\nu = 0$ points have been slightly shifted for convenience of plotting on a logarithmic scale. The lines show the theoretical predictions calculated by using the input model power spectrum $P^m(k)$ in eq. (24).

Results

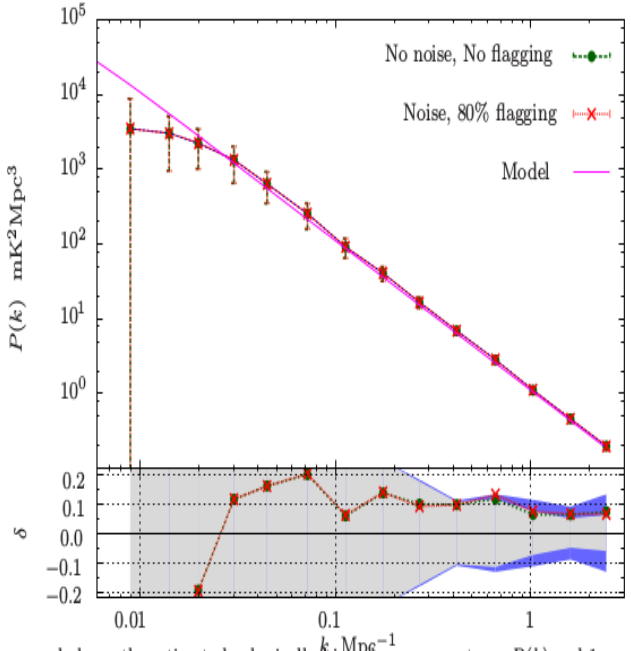

Figure 4. The upper panel shows the estimated spherically-binned power spectrum $P(k)$ and $1-\sigma$ error-bars for simulations with no noise and flagging and also with noise and 80% flagging. For comparison, the input model $P^m(k)$ is also shown by the solid line. The bottom panel shows the fractional error $\delta = [P(k) - P^m(k)]/P^m(k)$ (data points) and the relative statistical fluctuation $\sigma/P^m(k)$ (shaded regions). The values of σ are larger for simulations with noise and 80% flagging as compared to those with no noise and no flagging.

- P(k) for the simulations with no noise and no flagging, noise and 80% flagging, and the model power spectrum $P^m(k)$.
- P(k) under-estimated at $k < 0.02$ Mpc $^{-1}$ due to effect of convolution. Better agreement at $k \geq 0.02$ Mpc $^{-1}$.
- P(k) somewhat overestimated at $k \geq 0.03$ Mpc^{-1}, but difference goes down at larger k.

Results

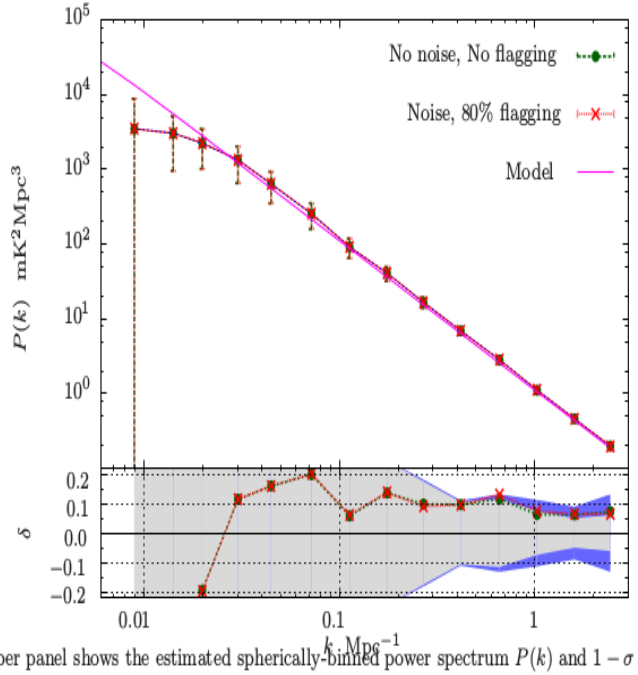

Figure 4. The upper panel shows the estimated spherically-binned power spectrum $P(k)$ and $1-\sigma$ error-bars for simulations with no noise and flagging and also with noise and 80% flagging. For comparison, the input model $P^m(k)$ is also shown by the solid line. The bottom panel shows the fractional error $\delta = [P(k) - P^m(k)]/P^m(k)$ (data points) and the relative statistical fluctuation $\sigma/P^m(k)$ (shaded regions). The values of σ are larger for simulations with noise and 80% flagging as compared to those with no noise and no flagging.

- $\delta = [P(k)\text{-}P^m(k)]/P^m(k)$, the shaded regions shows the $1-\sigma$ errors $\sigma/P^m(k)$.
- The values of σ are larger when we introduce noise and flagging, this is particularly more pronounced at large k.
- $P(k)$ is under-estimated by $10-20\%$ in the range $0.03 \leq k < 0.1$ Mpc^{-1}, $5-15\%$ in the range $0.1 \leq k < 1.0$ Mpc^{-1}, and $< 7.5\%$ at $k > 1.0$ Mpc^{-1}.
- In all cases we find that the errors δ are less than the expected statistical fluctuations $\sigma/P^m(k)$.

Demonstrating the Tapered Gridded Estimator (TGE) for the Cosmological HI 21-cm Power Spectrum using 150 MHz GMRT observations

Specifications for the Observation

Table 1. Observation summary

Central Frequency (ν_c)	153 MHz
Channel width ($\Delta\nu_c$)	62.5 kHz
Bandwidth (B_{bw})	8.00 MHz
Total observation time	11 hrs
Target field $(\alpha, \delta)_{2000}$	$(05^h30^m00^s, +60°00'00'')$
Galactic coordinates (l, b)	151.80°, 13.89°
Off source noise	1.3 mJy/Beam
Flux density (max., min.)	(905 mJy/Beam, −14 mJy/Beam)
Synthesized beam	$21'' \times 18''$, PA = 61°
Comoving distance at 153 MHz (r)	9231 Mpc
r' at 153 MHz (dr/dv)	16.99 Mpc/MHz

- Two sets of data used
- Point source removal
- Flux density of the brightest source observed in the field:

  Before point source subtraction: 905 mJy/beam

  After point source subtraction: 21 mJy/beam

For Details See Ghosh et al., 2012

Specifications for the Analysis

- No. of channels : 88
- Baseline range : 70-3000 λ
- 149860 baselines available
- Data flagged : 47%
- Gaussian window function : $e^{-\frac{\theta^2}{f^2\theta_0^2}}$
- f= 10.0, 2.0, 0.8, 0.6
- Realizations of UMAPS : 20
- Binned cylindrically

Results (MAPS)

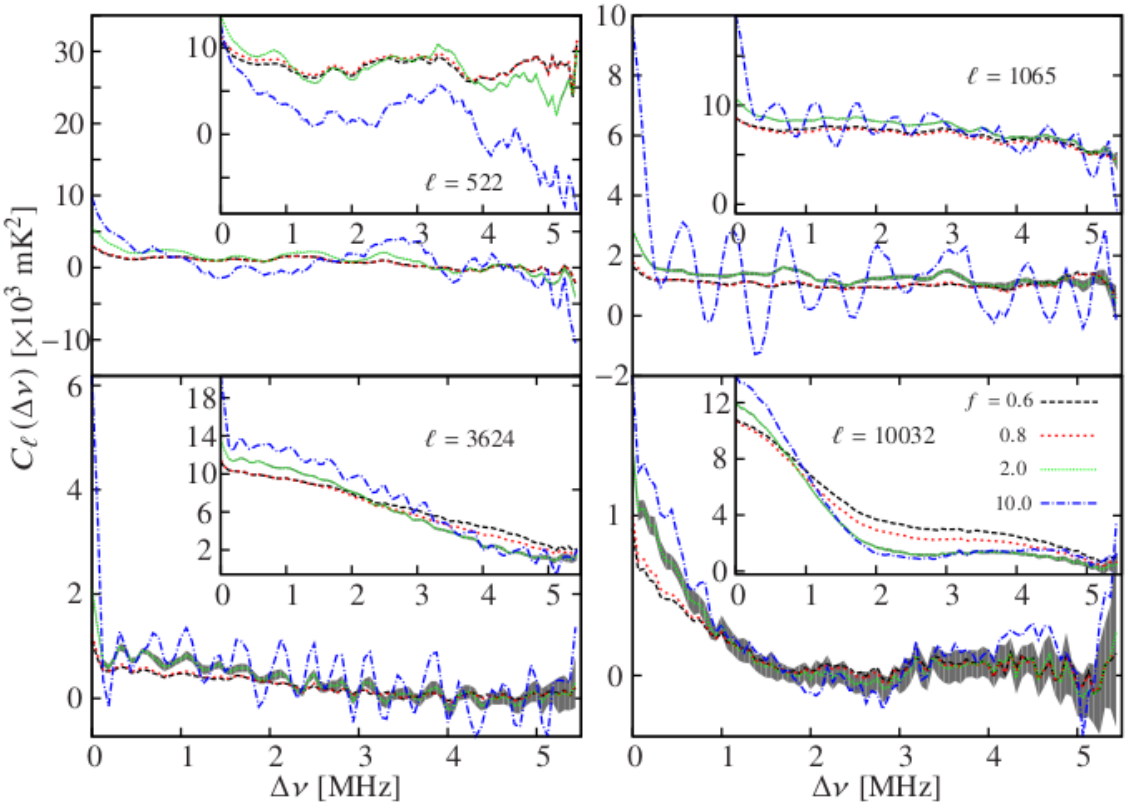

Figure 4. $C_\ell(\Delta\nu)$ as a function of $\Delta\nu$ after point source subtraction, with before point source subtraction shown as inset. The different panels correspond to different values of ℓ, and the different lines correspond to different f values as indicated in the legend. The black shaded regions for f = 2.0 displays the 10 σ error bars due to the system noise only.

- The estimated $C_\ell(\Delta\nu)$ remains correlated over 5.5 MHz at small ℓ's and decorrelates relatively faster at the larger ℓ bins.
- Considering any fixed ℓ bin, the decorrelation with $\Delta\nu$ is faster after the point sources have been subtracted.
- The overall amplitude of $C_\ell(\Delta\nu)$ falls approximately by one order of magnitude, especially at higher ℓ values when the point sources are removed.

Results (MAPS)

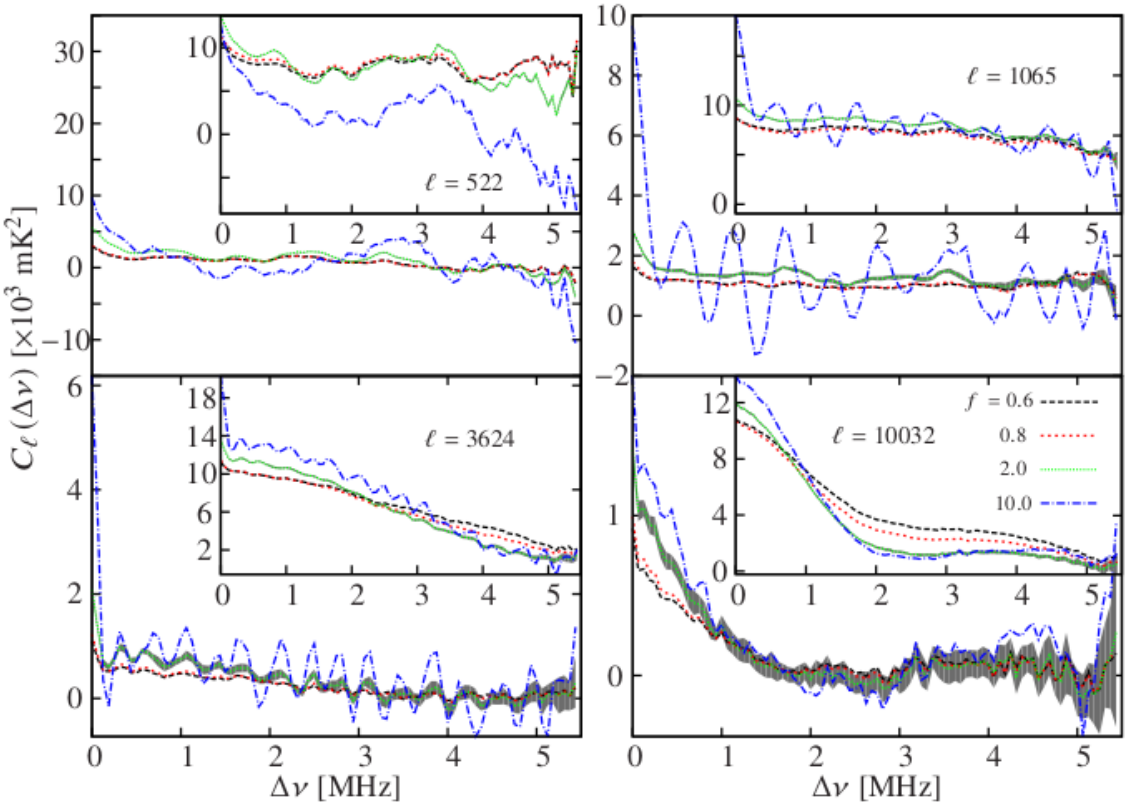

Figure 4. $C_\ell(\Delta\nu)$ as a function of $\Delta\nu$ after point source subtraction, with before point source subtraction shown as inset. The different panels correspond to different values of ℓ, and the different lines correspond to different f values as indicated in the legend. The black shaded regions for $f = 2.0$ displays the 10 σ error bars due to the system noise only.

$$[C_\ell(\Delta\nu)]_{\theta_1} \propto \cos(\ell\theta_1 \Delta\nu/\nu_c)$$

- An oscillatory pattern is observed at all angular scales for both sets of data due to the strong point sources located away from the phase center of the observations.
- The frequency of the oscillations is found to increase at larger baselines (higher ℓ values).

Results (MAPS)

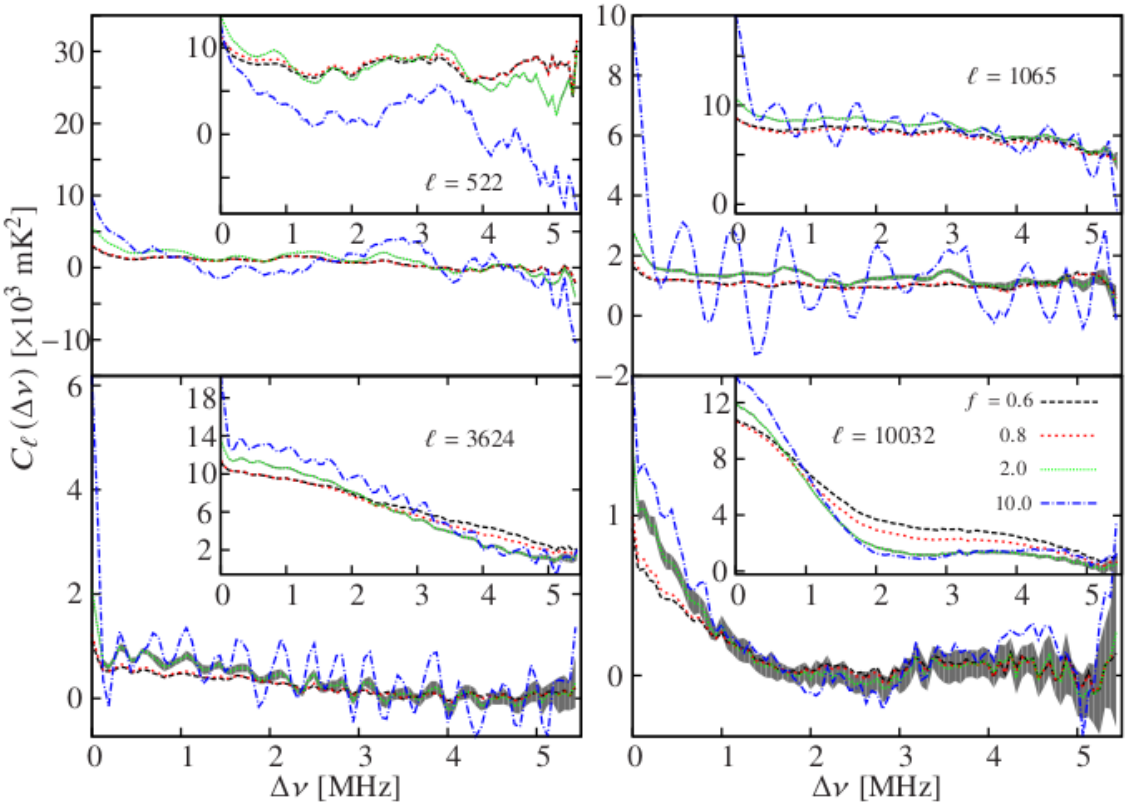

Figure 4. $C_\ell(\Delta\nu)$ as a function of $\Delta\nu$ after point source subtraction, with before point source subtraction shown as inset. The different panels correspond to different values of ℓ, and the different lines correspond to different f values as indicated in the legend. The black shaded regions for f = 2.0 displays the 10 σ error bars due to the system noise only.

- The tapering of the PB pattern suppresses the contributions from the outer parts of the FoV which brings down the amplitude of the oscillations.

- The tapering of the overall amplitude and the amplitude of the oscillations in the estimated$C_\ell(\Delta\nu)$, are more effective if we use the data after point source subtraction.

Results (Power Spectrum)

- MLE to estimate the power spectrum.
- Noise covariance matrix
- 20 linear bins along delay axis
- Foreground avoidance : Wedge, window, leakage

Results (Power Spectrum)

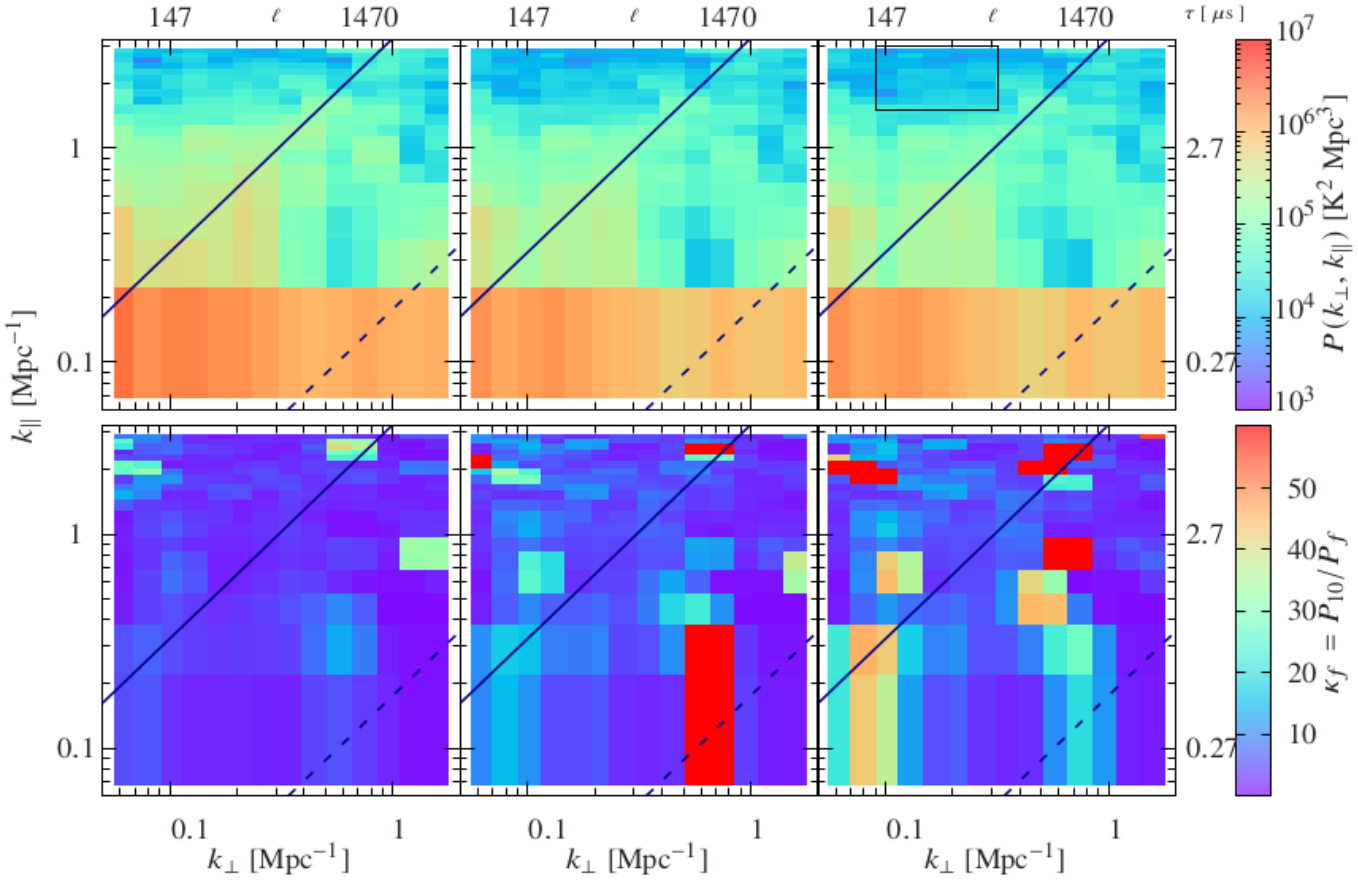

Figure 9. The upper row show the absolute value of the estimated cylindrical-binned power spectrum $P(k_\perp, k_\parallel)$ after point source subtraction for different tapering $f = 2.0, 0.8, 0.6$ (left to right panels). The lower row show the corresponding κ_f values. In all the cases, the solid and dashed lines respectively denote $[k_\parallel]_H$ and $[k_\parallel]_{\theta_1}$. Note that the $(k_\perp, k_\parallel)$ modes enclosed within the rectangular area indicated in the upper right panel at $f = 0.6$, have been binned in the later part of the section to obtain the spherically binned averaged power spectrum $P(k)$.

Results (Power Spectrum)

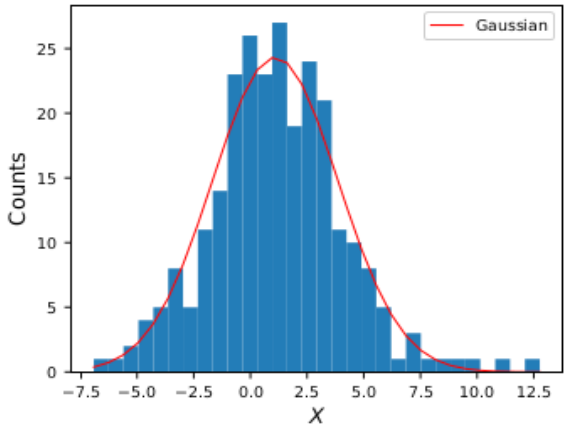

Figure 11. The histogram of the variable $X = \frac{P(k_\perp, k_\parallel)}{\delta P_N(k_\perp, k_\parallel)}$. The red line shows the Gaussian fit with mean 1.1 and standard deviation 2.77.

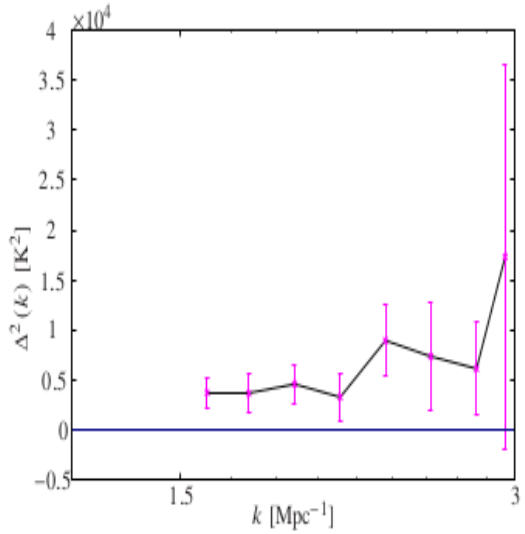

Figure 12. The mean square brightness temperature fluctuations $\Delta^2(k)$ shown as a function of k along with 2σ error bars.

Table 2. Estimated spherically binned mean square brightness temperature fluctuations $\Delta^2(k)$ and statistical error predictions σ for the same. The 2σ upper limits on $\Delta^2(k)$ ($\Delta^2_{UL}(k) = \Delta^2(k) + 2\sigma$) are listed corresponding to each k-bin.

k Mpc^{-1}	$\Delta^2(k)$ K^2 $= k^3 P(k)/2\pi^2$	σ K^2 $= k^3 \delta P/2\pi^2$	Upper limit, $\Delta^2_{UL}(k)$ (K)^2 $[2\sigma]$
1.59	$(61.47)^2$	$(27.40)^2$	$(72.66)^2$
1.73	$(60.70)^2$	$(31.61)^2$	$(75.38)^2$
1.90	$(67.96)^2$	$(30.74)^2$	$(80.68)^2$
2.09	$(57.61)^2$	$(34.75)^2$	$(75.72)^2$
2.30	$(94.74)^2$	$(42.47)^2$	$(112.17)^2$
2.52	$(85.93)^2$	$(51.53)^2$	$(112.67)^2$
2.78	$(78.50)^2$	$(47.85)^2$	$(103.64)^2$
2.94	$(131.75)^2$	$(98.00)^2$	$(191.22)^2$

Summary

- We have applied the estimator to estimate the MAPS and the Power spectrum of a heavily flagged GMRT observation at 153 MHz (z=8.28).

- No artefacts due to flagging are observed.

- This demonstrates that this estimator correctly estimates the noise bias and subtracts this out to yield an unbiased estimate of the power spectrum.

Summary

- The estimator successfully suppresses the foreground contributions by tapering the sky response at large angular separations from the phase center.
- Suppression depends on baseline distribution. In presence of denser uv-coverage we expect the suppression of foreground to be better.
- Given this data, we can put a $2-\sigma$ upper limit of $(72.66)^2$ K^2 on the mean squared HI 21-cm brightness temperature fluctuations at $k = 1.59$ Mpc^{-1} with the TGE.
- The data here is much too small for a detection. We next apply this new power spectrum estimation technique to more sensitive observations.

Towards 21-cm Intensity Mapping at z = 2.28 with uGMRT using the Tapered Gridded Estimator

Specifications for the Observation

Table 5.1: Observation summary

Working antennas	28
Central Frequency	400 MHz
Number of Channels	8192
Channel width	24.4 kHz
Bandwidth	200 MHz
Total observation time	25 hrs
Integration time	2 sec
Target field $(\alpha, \delta)_{2000}$	$(16^h10^m1^s, +54°30'36'')$
Galactic coordinates (l, b)	$86.95°, +44.48°$

Table 5.2: Considering the sub-band 2 with central frequency $\nu_c = 432.8$ MHz, spectral resolution $\Delta\nu_c = 24.4$ kHz and bandwidth $B_{bw} = 24.4$ MHz, we tabulate the flagging fraction and r.m.s. of the visibilities σ_N for different nights of observation

Night of observation	flag (%)	r.m.s. σ_N (Jy)
May 5	70.97	0.431337
May 6	13.07	0.394103
May 7	42.75	0.473156
May 27	71.29	0.445912
All nights combined	54.81	0.430112

- Flux density of the brightest source observed in the field after point source subtraction: 100 microJy/beam

For Details See Chakraborty et al. (2019a,b)

Specifications for the Observation

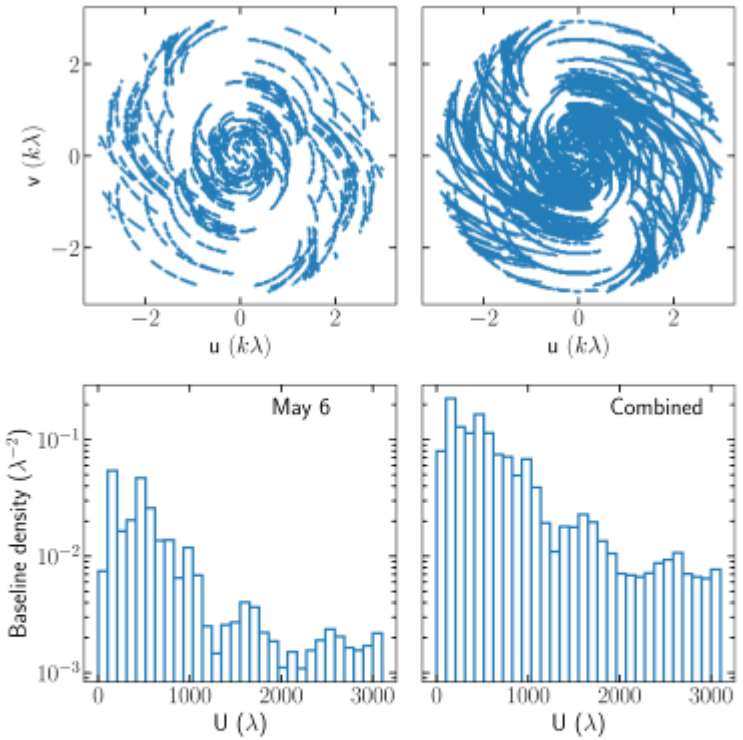

Figure 5.1: The upper panels show the uv-coverage for the May 6 data (left panel) and the combined nights data (right panel) considering baselines of length $U \leq 3000\lambda$ at $\nu_c = 432.8\,\mathrm{MHz}$. The corresponding baseline density (number of baselines per unit area of the uv plane) are shown as a function of U in the lower panels.

Results (MAPS)

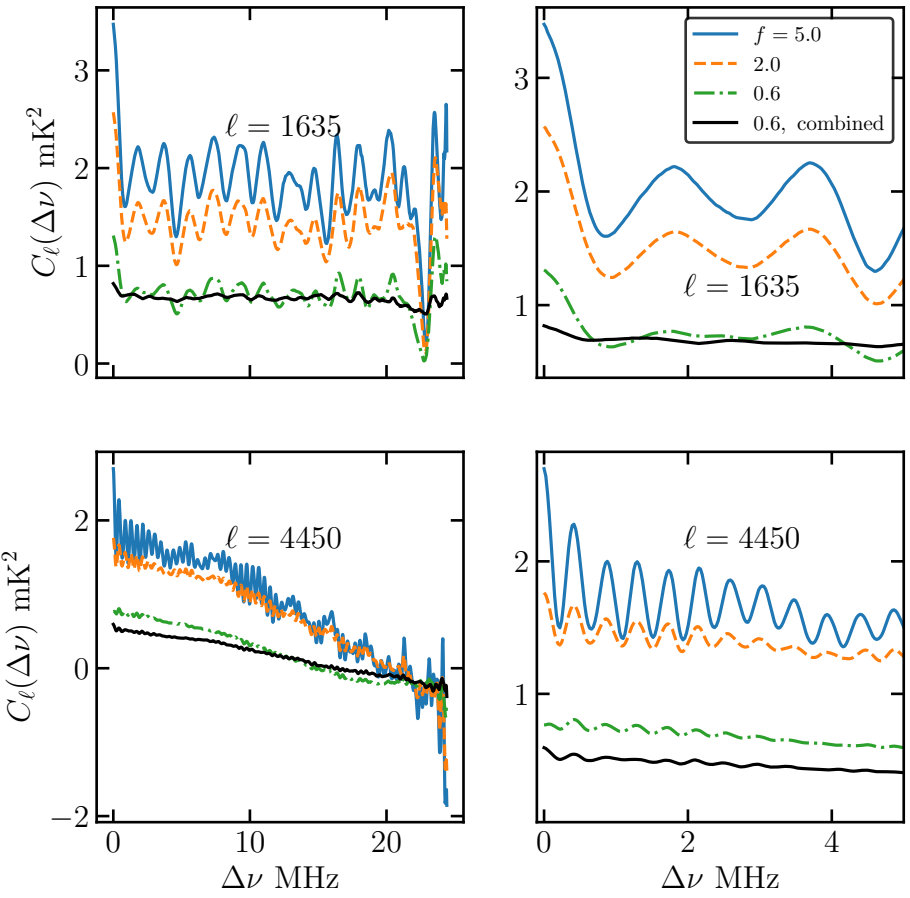

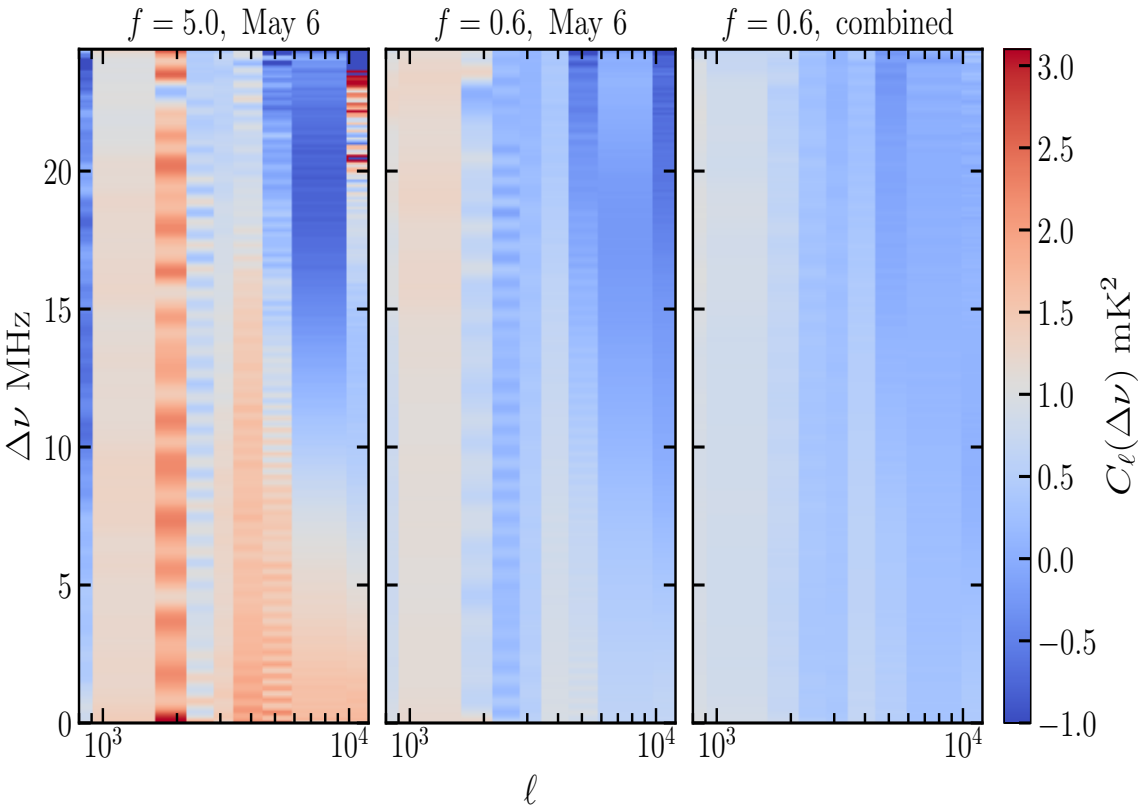

$$[C_\ell(\Delta\nu)]_{\theta_1} \propto \cos(\ell\theta_1\,\Delta\nu/\nu_c)$$

Results (Power Spectrum)

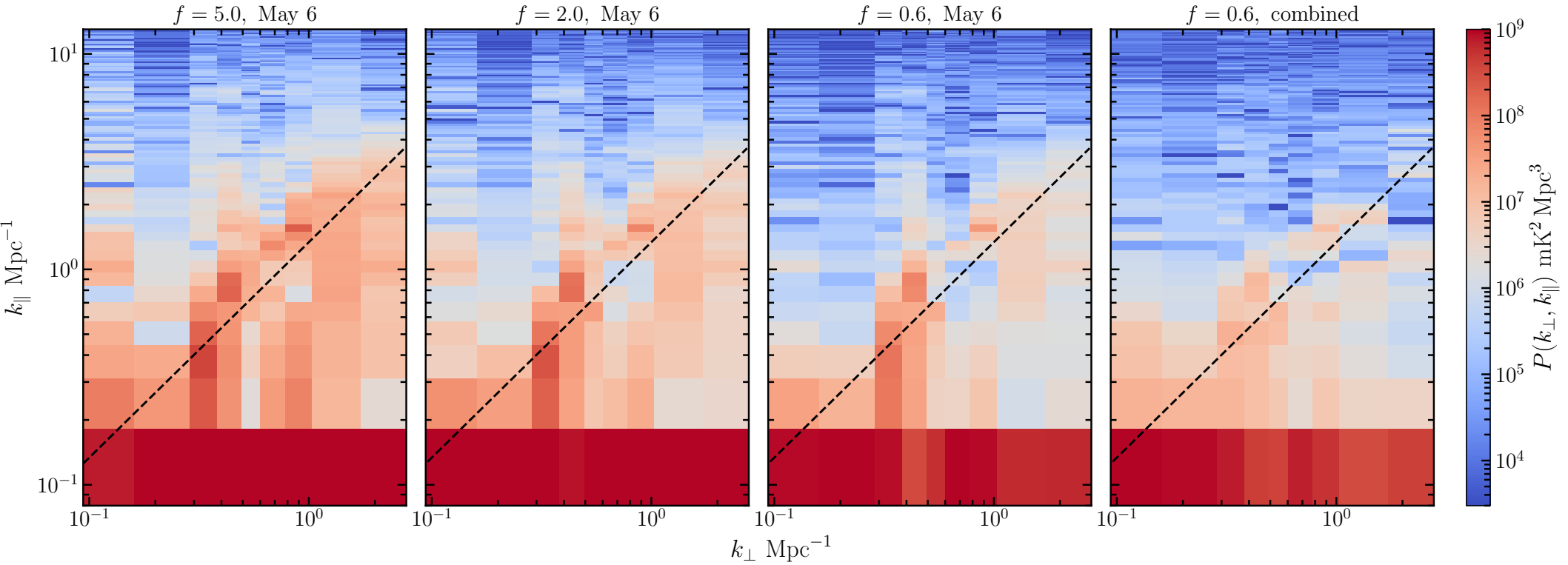

Results (Power Spectrum)

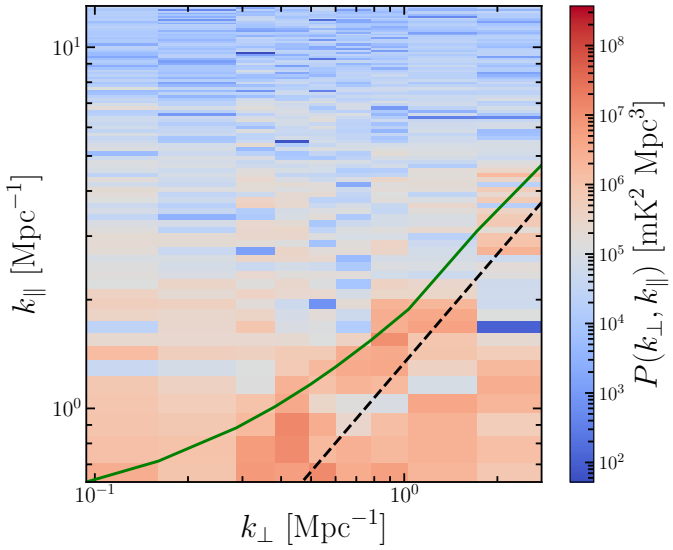

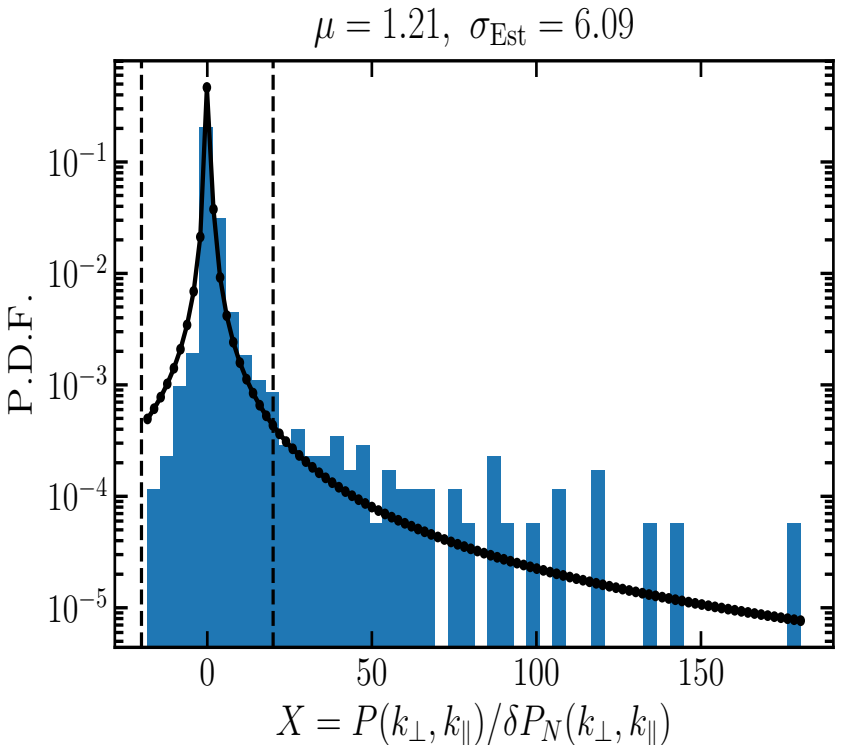

Results (Power Spectrum)

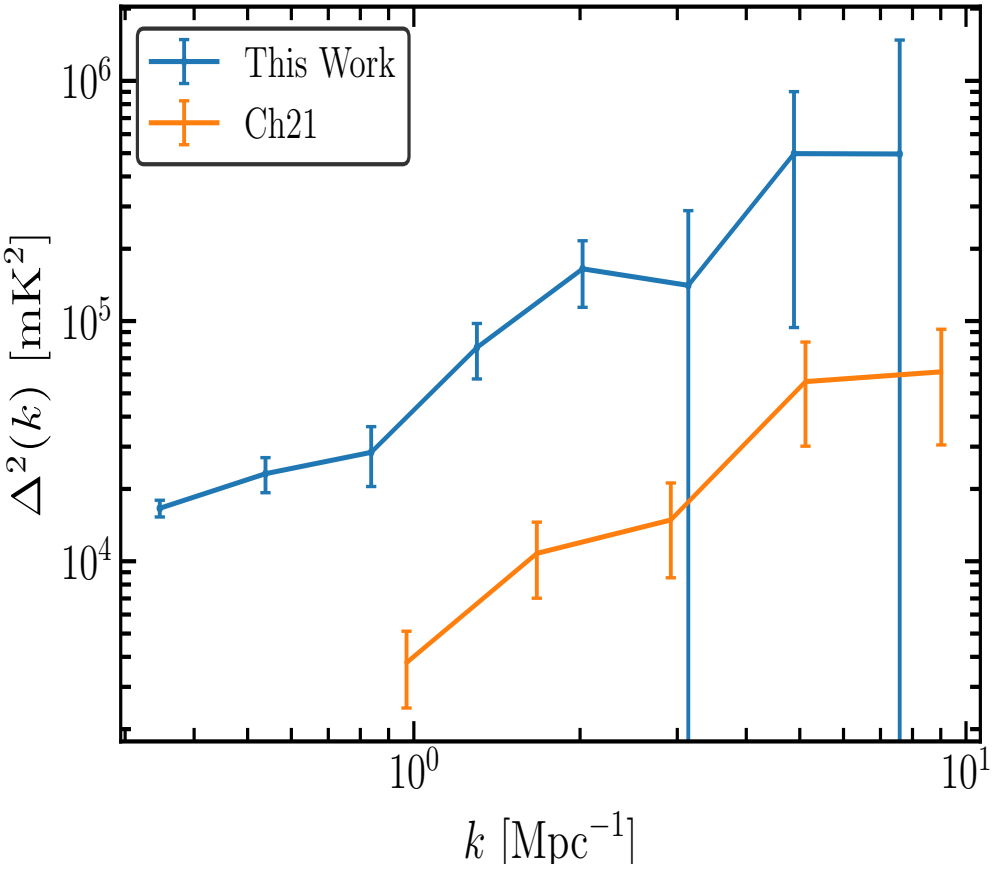

$$P_T(\boldsymbol{k}) = [\Omega_{\rm HI} b_{\rm HI}]^2 \bar{T}^2 P_m^s(\boldsymbol{k})$$

Table 3. Spherically binned mean square brightness temperature fluctuations $\Delta^2(k)$ and the corresponding statistical error predictions σ for different k-bins. The 2 σ upper limits $\Delta^2_{UL}(k) = \Delta^2(k) + 2\,\sigma$ and corresponding $[\Omega_{\rm HI}\, b_{\rm HI}\,]_{UL}$ values are also provided.

k Mpc^{-1}	$\Delta^2(k)$ (mK)^2	1σ (mK)^2	$\Delta^2_{UL}(k)$ (mK)^2	$[\Omega_{\rm HI}\, b_{\rm HI}\,]_{UL}$
0.347	$(128.91)^2$	$(25.79)^2$	$(133.97)^2$	0.230
0.539	$(152.14)^2$	$(43.92)^2$	$(164.33)^2$	0.234
0.837	$(168.54)^2$	$(62.99)^2$	$(190.64)^2$	0.230
1.301	$(278.48)^2$	$(100.37)^2$	$(312.57)^2$	0.326
2.021	$(406.20)^2$	$(159.58)^2$	$(464.68)^2$	0.425
3.141	$(375.19)^2$	$(271.49)^2$	$(536.83)^2$	0.436
4.881	$(705.60)^2$	$(449.38)^2$	$(949.61)^2$	0.694
7.584	$(704.35)^2$	$(701.07)^2$	$(1216.18)^2$	0.807

- Ch21, $\Delta^2{}_{\rm UL}(k) \leq (61.49)^2$ mK^2 and $[\Omega_{\rm HI}\, b_{\rm HI}]_{\rm UL} \leq 0.11$ at k = 1 Mpc^{-1}.

Results (Power Spectrum)

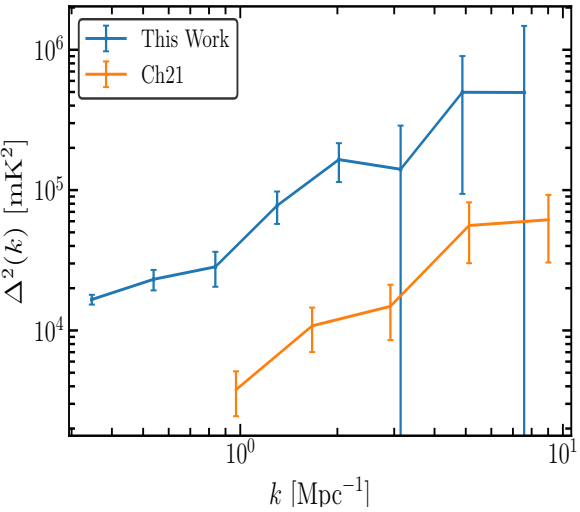

Pal S et al., 2022

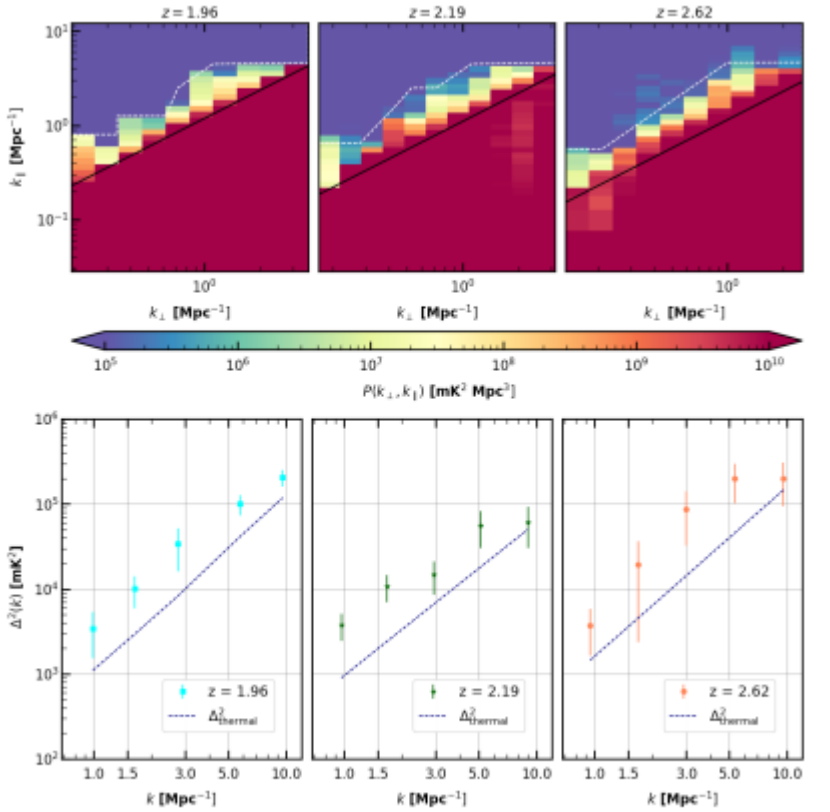

Figure 5. The cylindrically averaged 2D power spectrum (upper panel) and spherically averaged 3D power spectrum (lower panel) for redshifts $z = 1.96$ (left column), 2.19 (middle column) and 2.62 (right column).

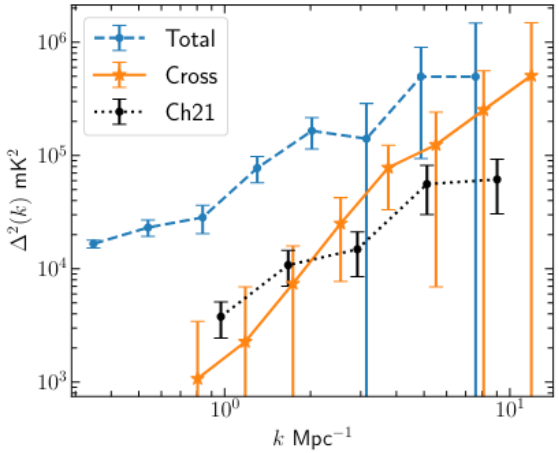

Figure 8. The mean squared brightness temperature fluctuations $\Delta^2(k)$ along with 2σ error bars. The orange asterisks show the results from the present work (Cross), while the blue dashed and black dotted lines show the results from Paper I (Total) and Ch21, respectively.

Elahi A et al., 2023

Chakraborty A et al., 2021

$$[\Omega_{\rm HI}\, b_{\rm HI}]_{\rm UL} \leq 0.061 \text{ at } k = 0.8 \text{ Mpc}^{-1}$$

$$\hat{E}_g(\nu_a, \nu_b) = M_g^{-1}(\nu_a, \nu_b)\mathcal{R}\left[V_{cg}^{XX}(\nu_a)V_{cg}^{*YY}(\nu_b) + V_{cg}^{YY}(\nu_a)V_{cg}^{*XX}(\nu_b)\right]$$

Foreground Removal

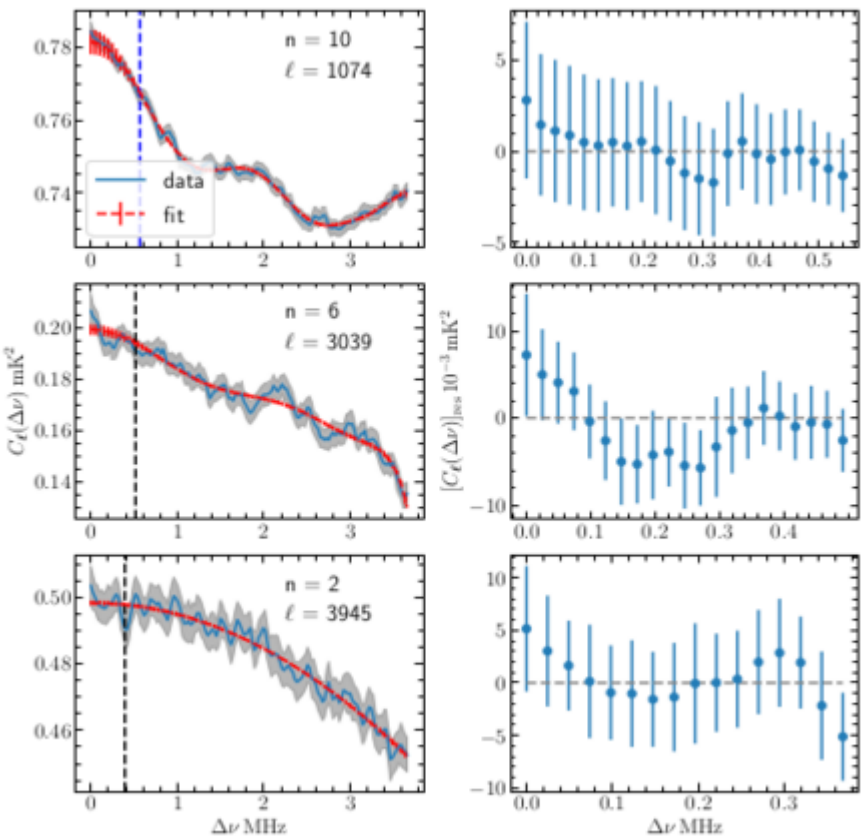

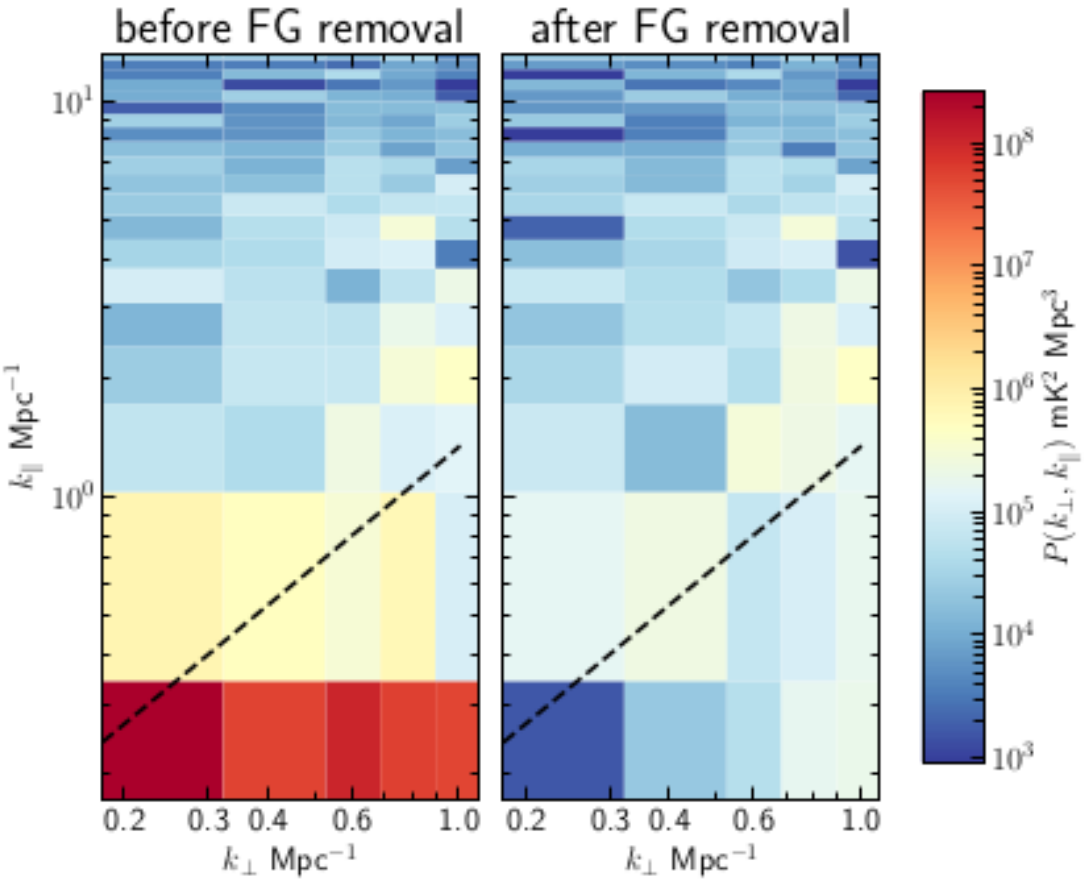

$[\Omega_{HI}\, b_{HI}]_{UL} \leq 0.022$ at $k = 0.247$ Mpc^{-1}

Elahi et al., 2023

Summary

- We have applied the TGE estimator to estimate the MAPS and the Power spectrum of a heavily flagged uGMRT observation at 153 MHz (z=2.28).

- No artefacts due to flagging are observed.

- The effect of tapering in the estimated $C_\ell(\Delta\nu)$ and P $(k_\perp, k_{||})$ for this data is same as what we observed in the previous data. This demonstrates that the TGE is effective in tapering the sky response to suppress the contribution from sources in the outer region of the FoV.

Summary

- Comparing the combined nights with an individual night data having same degree of tapering f=0.6, we find that the oscillations and the overall amplitude of $C_\ell(\Delta\nu)$ is even further reduced when we consider the combined nights data.

- The combined nights data has the higher baseline density which makes the tapering more effective than an individual night data. Similarly, in P ($k_\perp$, $k_{||}$) overall foreground amplitude and also the foreground leakage outside the wedge both are further reduced for the combined nights data.

Summary

- We find the tightest 2σ upper limit of $\Delta^2_{UL}(k) \leq (18.07)^2\ mK^2$ at $k = 0.247\ Mpc^{-1}$ which translates to an upper limit $[\Omega_{HI}\ b_{HI}]_{UL} \leq 0.022$ after using foreground removal.

- The upper limits presented here are still around 10 times larger than the expected signal corresponding to $\Omega_{HI} \sim 10^{-3}$ and $b_{HI} \sim 2$.

Concluding Remarks

- We have presented an estimator for the detection of the 21-cm MAPS and power spectrum from EoR and post-EoR from radio interferometric observations.
- We have validated the estimator using simulations.
- We have demonstrated the salient features of the TGE.
- We could constrain 2σ upper limit of $\Delta^2_{UL}(k) \leq (18.07)^2$ mK^2 at $k = 0.0247$ Mpc^{-1} which translates to an upper limit $[\Omega_{HI}\, b_{HI}]_{UL} \leq 0.022$ at $z=2.28$.

Thank You !!!!